

1 Quantitative modeling of the emergence of
2 macroscopic grid-like representations

3 Ikhwan Bin Khalid^{1,2,*}, Eric T. Reifenstein^{1,2,3,*}, Naomi Auer², Lukas Kunz^{4,+}, and
4 Richard Kempter^{1,2,5,+}

5 ¹Bernstein Center for Computational Neuroscience Berlin, Philippstr. 13, D-10115
6 Berlin

7 ²Institute for Theoretical Biology, Department of Biology, Humboldt-Universität zu
8 Berlin, Philippstr. 13, D-10115 Berlin

9 ³Department of Mathematics and Computer Science, Freie Universität Berlin,
10 Arnimallee 3, D-14195 Berlin

11 ⁴Department of Biomedical Engineering, Columbia University, New York, NY, USA

12 ⁵Einstein Center for Neurosciences Berlin, Charitéplatz 1, D-10117 Berlin

13 *Co-first authors

14 +Co-last authors

15 December 20, 2022

16 Correspondence should be addressed to:

17
18 Lukas Kunz
19 Department of Biomedical Engineering
20 Columbia University
21 New York, NY, USA
22 Email: lukas.kunz@columbia.edu

23
24 Richard Kempter
25 Department of Biology, Institute for Theoretical Biology
26 Humboldt-Universität zu Berlin
27 Philippstr. 13, D-10115 Berlin, Germany
28 Phone: +49-(0)30-2093-98404
29 Email: r.kempter@biologie.hu-berlin.de

31 **Abstract**

32 Grid cells are neurons in the entorhinal cortex that play a key role in spatial navigation. When subjects
33 navigate through spatial environments, grid cells exhibit firing fields that are arranged in a triangular
34 grid pattern. As direct recordings of grid cells from the human brain are only rarely possible, functional
35 magnetic resonance imaging (fMRI) studies proposed and described an indirect measure of entorhinal
36 grid-cell activity, which is quantified as a hexadirectional modulation of fMRI activity as a function of
37 the subject's movement direction. However, it still remains unclear how the activity of single grid cells is
38 related to the sum activity of a population of grid cells, which may exhibit hexadirectional modulation
39 and thus provide the basis for the hexadirectional modulation of entorhinal cortex activity measured with
40 fMRI. Here, we thus performed numerical simulations and analytical calculations to better understand
41 how the aggregated activity of many grid cells may be hexadirectionally modulated. Our simulations
42 implemented three different hypotheses proposing that the hexadirectional modulation occurs because
43 grid cells show head-direction tuning aligned with the grid axes; are subjected to repetition suppression;
44 or exhibit a bias towards a particular grid phase offset. Our simulations demonstrate that all three
45 hypotheses can, in principle, lead to a hexadirectional modulation of sum grid-cell activity. However, the
46 magnitude of the hexadirectional modulation appears to depend considerably on the subject's navigation
47 pattern and the exact biological properties of grid cells. Our results thus indicate that future fMRI studies
48 could be designed to test which of the three hypotheses most likely accounts for the fMRI measure of
49 grid cells. These findings also underline the importance of quantifying the biological properties of single
50 grid cells in humans to further elucidate how hexadirectional modulations of fMRI activity may emerge.

1 Introduction

The neural basis of spatial navigation comprises multiple specialized cell types such as place cells (O’Keefe and Dostrovsky, 1971), head-direction cells (Taube et al., 1990), and grid cells (Hafting et al., 2005), whose activity profiles result from intricate mechanisms of microcircuits in the medial temporal lobes (Tukker et al., 2022). Grid cells are neurons that activate whenever an animal or human traverses the vertices of a triangular grid tiling the entire environment into equilateral triangles (Hafting et al., 2005; Jacobs et al., 2013). Grid cells may allow the navigating organism to perform vector computations and may thus constitute an essential neural substrate for different types of spatial navigation including path integration (Stemmler et al., 2015; Bush et al., 2015; Moser et al., 2017; Stangl et al., 2018; Gil et al., 2018; Banino et al., 2018; Bierbrauer et al., 2020).

In rodents, grid cells can be recorded using electrodes inserted into the medial entorhinal cortex (EC). In humans, measuring grid cells using invasive methods is only rarely possible, for example, by recording single-neuron activity in epilepsy patients who are neurosurgically implanted with intracranial depth electrodes (Jacobs et al., 2013; Nadasdy et al., 2017). Hence, to enable the detection of grid cells in healthy humans, a functional magnetic resonance imaging (fMRI) method has been developed that tests for a hexadirectional modulation of the blood-oxygen-level-dependent (BOLD) signal as a function of the subject’s movement direction through a virtual environment (Doeller et al., 2010). We here refer to this phenomenon of a hexadirectional modulation of the fMRI signal as “macroscopic grid-like representations”, which has been replicated repeatedly in recent years (e.g. Kunz et al., 2015; Bellmund et al., 2016; Horner et al., 2016; Constantinescu et al., 2016; Bierbrauer et al., 2020). The mechanisms underlying the emergence of such macroscopic grid-like representations remain still unclear, however.

To provide possible explanations for the emergence of macroscopic grid-like representations, previous studies presented several qualitatively different hypotheses on how the activity of single grid cells translates into a macroscopically visible hexadirectional fMRI signal (Doeller et al., 2010; Kunz et al., 2019). Three main hypotheses have been developed: (i) the “conjunctive grid by head-direction cell hypothesis”; (ii) the “repetition suppression hypothesis”; and (iii) the “structure-function mapping hypothesis” (Fig. 1).

The conjunctive grid by head-direction cell hypothesis builds on the finding that the firing of conjunctive grid by head-direction cells located in deeper layers of the entorhinal cortex and in pre- and parasubiculum (Sargolini et al., 2006) is aligned with the grid axes (Doeller et al., 2010). Assuming that the directional tuning width of these conjunctive grid by head-direction cells is not too broad, movements aligned with the grid axes (as compared to misaligned movements) result in increased spiking activity of the conjunctive grid by head-direction cell population. Given some correlation between population spiking activity and the fMRI signal, this systematic difference in the firing of conjunctive grid by head-direction cells when moving aligned versus misaligned with the grid axes may thus cause a macroscopically visible fMRI signal with hexadirectional modulation (Fig. 1B).

The repetition suppression hypothesis (Fig. 1C) is based on the assumption that the phenomenon of repetition suppression—i.e., neural activity being reduced for repeated stimuli (Grill-Spector et al., 2006)—also applies to grid cells (Doeller et al., 2010; Killian et al., 2012). Critical to this hypothesis is that relatively fewer different grid cells are activated more often during movements aligned with the grid axes, and relatively more different grid cells are activated less often during misaligned movements. Due to this systematic difference in how many grid cells are activated how often, a higher degree of repetition suppression at the level of spiking activity or the fMRI signal (i.e., fMRI adaptation) during aligned movements as compared with misaligned movements can emerge, again resulting in a hexadirectional modulation of fMRI activity as a function of the subject’s movement direction through the spatial environment.

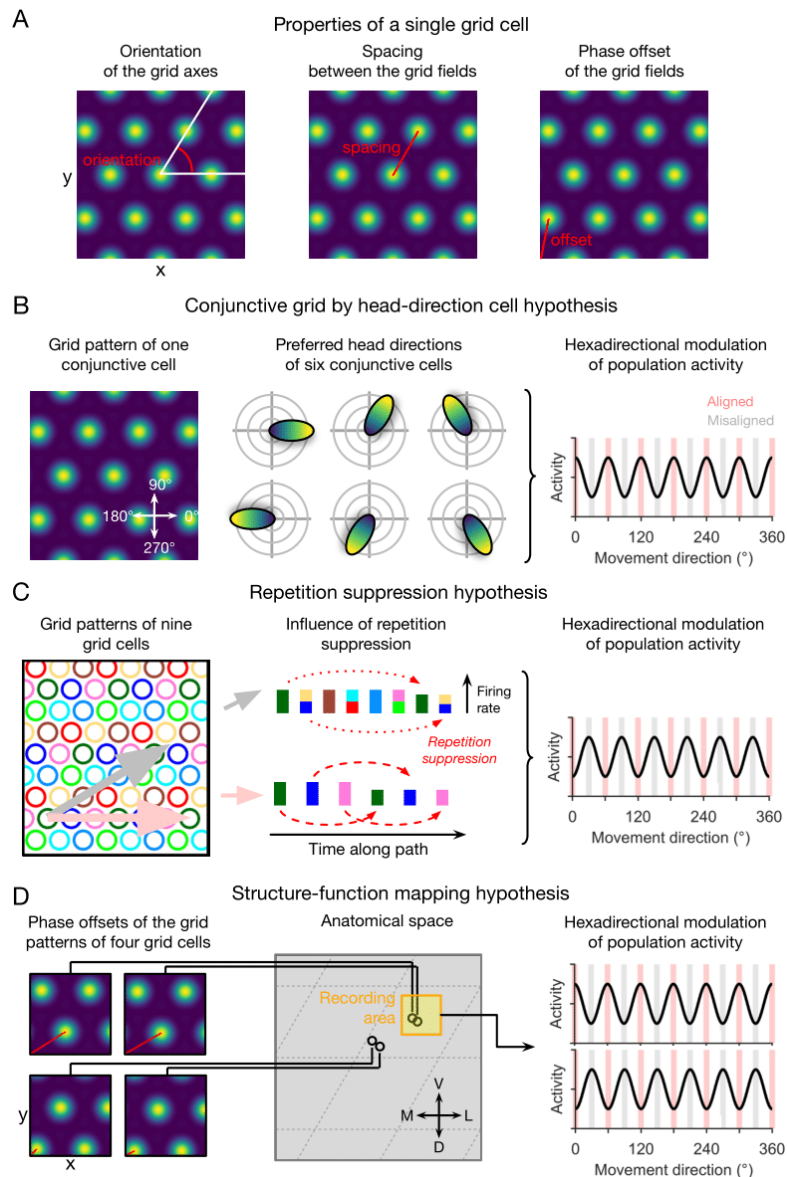


Figure 1: Qualitative hypotheses on the emergence of macroscopic grid-like representations in the human entorhinal cortex (adapted from Kunz et al., 2019). (A) Grid-cell properties comprise grid orientation, grid spacing, and grid phase offset. (B) Macroscopic grid-like representations (right) may emerge from the firing of conjunctive grid by head-direction cells (left and middle) that exhibit increased firing when the subject moves aligned as compared to misaligned with the grid axes (right) (Doeller et al., 2010). (C) In a grid cell population with similar grid orientations and grid spacings but with distributed phases (left; colored circles represent firing fields of different grid cells), aligned movements (horizontal pink arrow) lead to more frequent activation (shorter distance between firing fields) of a smaller number of different grid cells, whereas misaligned movements (diagonal gray arrow) lead to less frequent activation (larger distance between firing fields) of a higher number of different grid cells (Doeller et al., 2010). Thus, aligned movements may lead to more pronounced repetition suppression as compared to misaligned movements (middle), resulting in a hexadirectional modulation of population spiking activity and thus in the emergence of grid-like representations (right). (D) Because anatomically adjacent grid cells exhibit similar grid phase offsets (in addition to similar grid orientations and grid spacings) (Gu et al., 2018), recordings from a limited number of grid cells with a non-random distribution of phase offsets may lead to macroscopic grid-like representations. The left panel shows the grid phase offset of four different grid cells, whose anatomical locations are illustrated in the middle panel. Depending on the subject's starting location relative to the phase offset of the grid fields, movements aligned or misaligned with the grid axes lead to higher sum grid cell activity as compared to misaligned or aligned movements (right panel). D, dorsal; L, lateral; M, medial; V, ventral.

97 Regarding the structure–function mapping hypothesis (Fig. 1D), studies in rodents have demonstrated
98 that the firing fields of anatomically adjacent grid cells do not only have similar spacing and orientation
99 (Stensola et al., 2012), but also a similar grid phase offset to a reference location (Heys et al., 2014; Gu
100 et al., 2018). Therefore, recordings from a small area of the entorhinal cortex (e.g. a sufficiently small
101 voxel of an fMRI scan) may sample grid cells with similar firing fields, which basically behave like a
102 single grid cell. It has been suggested that such a grid cell population might show higher average firing
103 rates during aligned movements (because more firing fields are traversed) versus misaligned movements,
104 again resulting in macroscopically visible grid-like representations (Kunz et al., 2019).

105 In this study, we aimed at quantitatively evaluating the three hypotheses on the emergence of macro-
106 scopic grid-like representations using a modeling approach. Our results show that all three hypotheses
107 can result in macroscopic grid-like representations under ideal and specific conditions, but the magnitude
108 of the hexadirectional modulation varies by orders of magnitude. Key findings are that the subjects’
109 type of navigation paths through the spatial environments and the exact biological characteristics of grid
110 cells determine how much a given hypothesis contributes to a hexadirectional population signal in the
111 entorhinal cortex. In this way, our results help understand how grid cells may have a specific correlate in
112 fMRI, make predictions on how future fMRI studies could establish evidence in favor of one of the three
113 hypotheses, and suggest that the biological properties of grid cells in humans should be investigated in
114 greater detail in order to support or weaken the plausibility of either of the three hypotheses.

115 2 Results

116 2.1 Navigation strategies

117 To evaluate the different hypotheses on the emergence of grid-like representations, we considered three
118 different types of navigation trajectories: “star-like walks”, “piecewise linear walks”, and “random walks”.
119 We opted for this approach in order to test whether a subject’s navigation pattern—which in itself
120 comes with a certain degree of hexasymmetry (“path hexasymmetry”)—influences the emergence of
121 hexadirectional sum signals of neuronal activity.

122 During each path segment of star-like walks, the simulated agent started from the same (x/y)-
123 coordinate and navigated along one of 360 predefined allocentric navigation directions (0° to 359° in
124 steps of 1° ; Fig. 2B). This ensured that the navigation trajectory itself exhibited a hexasymmetry that
125 was essentially zero. Each path had a length of 300 cm, which was ten times the grid scale (see Table 1
126 for a summary of all model parameters). After each path segment, the agent was “teleported” back to
127 the initial (x/y)-coordinate and completed the next path segment. For real-world experiments, this type
128 of navigation including teleportation is unusual, but it can be implemented in virtual-reality experiments
129 (Vass et al., 2016; Deuker et al., 2016).

130 During piecewise linear walks, the subject also completed 360 path segments of 300 cm length along
131 the same 360 predefined allocentric navigation directions, as in the star-like walks. In this case, however,
132 the path segments were “unwrapped” such that the starting location of a path segment was identical with
133 the end location of the preceding path segment (Fig. 2C). The sequence of allocentric navigation directions
134 was randomly chosen. As for star-like walks, piecewise linear walks do not exhibit hexasymmetry *a priori*.
135 Piecewise linear walks are commonly seen in virtual-reality and real-world navigation tasks in humans—
136 in particular when subjects are asked to navigate between different goal locations (Doeller et al., 2010;
137 Kunz et al., 2015; Horner et al., 2016).

138 For random walks, we modeled navigation trajectories following (Kropff and Treves, 2008; Si et al.,
139 2012; D’Albis and Kempter, 2017)(for details, see Methods around Eq. (1)), which allowed us to vary the
140 tortuosity of the paths. For a certain value of the tortuosity parameter ($\sigma_\theta = 0.5 \text{ rad/s}^{1/2}$) and a time

141 step $\Delta t = 0.01$ s, this led to navigation paths that we considered similar to those seen in rodent studies
142 (Fig. 2D; Fig. S2E). Apart from random walks in basically infinite environments, we also simulated
143 random walks in finite enclosures (circles and squares) with different sizes and orientations; we found
144 that these restrictions had a negligible effect on path hexasymmetry (Figs. S5C and S6C). Because the
145 allocentric navigation directions are not predefined for random walks, they exhibit varying degrees of path
146 hexasymmetry. The longer the simulated random walks, the smaller the path hexasymmetry (Fig. S1);
147 we simulated random walks with a total length of typically 900 m ($M = 9 \cdot 10^5$ steps).

148 As we describe below, the emergence of grid-like representations based on the conjunctive hypothesis
149 is robust against the specific type of navigation strategy, whereas the other two hypotheses are sensitive
150 to particular navigation strategies. Future studies on hexadirectional signals should thus consider the
151 kind of navigation paths subjects will use during a given task.

152 2.2 Quantifying neural hexasymmetry generated by the three hypotheses

153 To test how the activity of grid cells could give rise to hexasymmetry of a macroscopic signal, we used a
154 firing-rate model of grid cell activity (Eq. 2). Furthermore, we developed a new measure H to quantify
155 neural hexasymmetry (Eq. 12), which is the magnitude of the hexadirectional modulation of the summed
156 activity of many cells (for details, see Methods).

157 2.2.1 Conjunctive grid by head-direction cell hypothesis

158 The conjunctive grid by head-direction cell hypothesis (Doeller et al., 2010) suggests that hexadirectional
159 activity in the entorhinal cortex emerges due to grid cells whose firing rate is additionally modulated by
160 head direction, whereby the preferred head direction is closely aligned with one of the grid axes (Fig. 2A).
161 By modulating the activity of individual grid cells with a head-direction tuning term (Methods, Eq. 3),
162 our simulations indeed showed that these properties resulted in a clear hexadirectional modulation of
163 sum grid-cell activity (Fig. 2, B–D). When considering different types of navigation trajectories, we found
164 that they led to similar distributions of sum grid cell activity as a function of movement direction and,
165 accordingly, to similar hexasymmetry values (Fig. 2, B–D). In all three cases, the directions of maximal
166 activity were aligned with the grid axes.

167 These results were obtained using ideal values for the preciseness of the head-direction tuning (i.e., the
168 concentration parameter of head-direction tuning, κ_c) and the alignment of the preferred head directions
169 to the grid axes (i.e., the alignment jitter of the head-direction tuning to the grid axes, σ_c ; Fig. 2A). We
170 were thus curious how the hexasymmetry changed when using a wide range of parameter values that
171 would also include biologically plausible values. We varied κ_c between values corresponding to narrow
172 tuning widths ($\kappa_c = 50 \text{ rad}^{-2}$, which corresponds to an angular variability of $1/\sqrt{\kappa_c} \approx 8^\circ$) and wide
173 tuning widths ($\kappa_c = 10 \text{ rad}^{-2}$, i.e. an angular variability of approximately 18°), and σ_c between values
174 of no jitter ($\sigma_c = 0$) and significant jitter ($\sigma_c = 3^\circ$). We found that a combination of narrow head
175 direction tuning widths and no jitter resulted in the largest hexasymmetry H (Fig. 2, E–H), while wider
176 tuning widths with non-zero jitter resulted in smaller values for the hexasymmetry. Still, even if using
177 non-ideal, biologically plausible parameters (Doeller et al., 2010), the hexasymmetries were relatively
178 large compared to those from the repetition-suppression and the structure-function mapping hypotheses
179 (see below).

180 2.2.2 Repetition suppression hypothesis

181 Next, we performed simulations to understand whether the repetition suppression hypothesis (Doeller
182 et al., 2010) results in a hexadirectional modulation of population grid-cell activity. This hypothesis

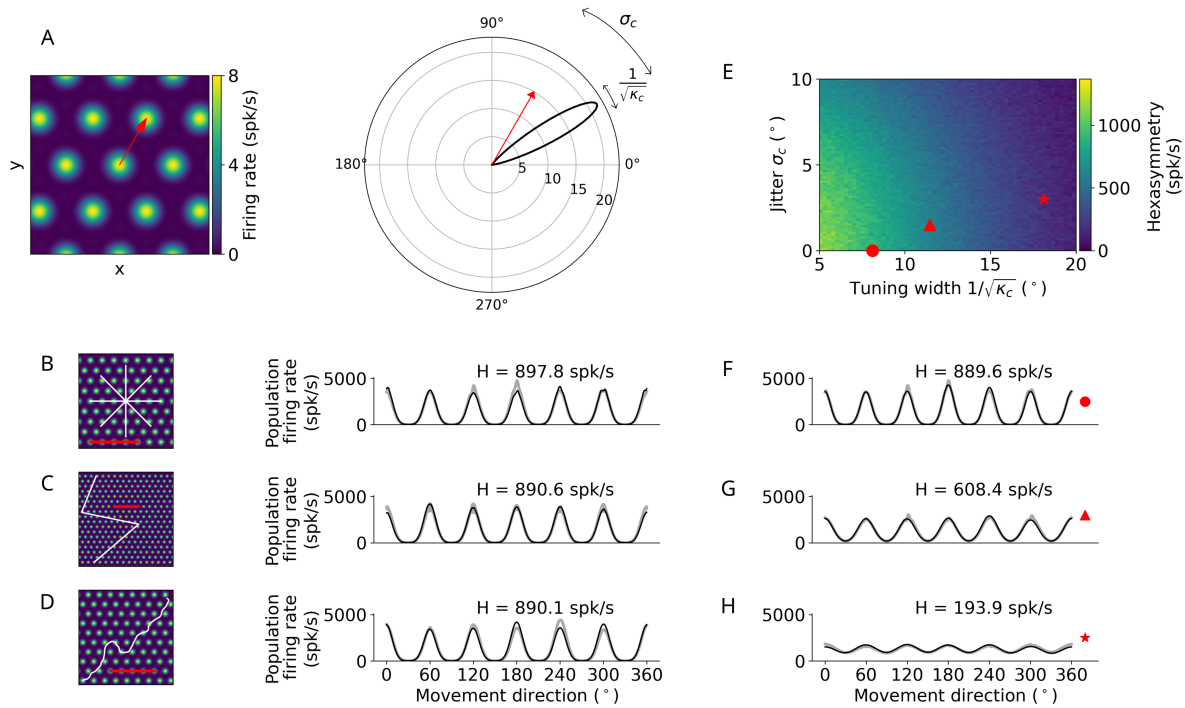


Figure 2: Conjunctive grid by head-direction cell hypothesis. (A) Grid tuning (left) and head-direction (HD) tuning (right) of a single conjunctive cell. Given experimental findings (Doeller et al., 2010), the preferred head direction aligns with one of the three axes of the grid. Two factors add noise to this relation: the HD tuning has a certain width ($\sqrt{1/\kappa_c}$) and the alignment of grid orientation to HD tuning angle is jittered (σ_c). (B–D) Simulation of the conjunctive hypothesis using “ideal” parameters of $\kappa_c = 50$ rad⁻² and $\sigma_c = 0^\circ$. The scale bars (red) represent a distance of 120 cm. (B) Left: Illustration of a star-like walk (path segments are cut for illustration purposes), overlaid onto the firing pattern of a single grid cell. Right: Population firing rate as a function of the subject’s movement direction (which is identical with head direction in our simulations) for star-like runs with mean firing rate $\bar{A}_0 = 1279.7$ spk/s (for 1024 cells) and path hexasymmetry $|\bar{T}_6| < 10^{-10}$; see Methods for definitions of \bar{A}_0 and \bar{T}_6 . (C) Left: Illustration of a piece-wise linear walk (cut for illustration purposes), overlaid onto the firing pattern of a single grid cell. Right: Population firing rate as a function of movement direction for piece-wise linear walks with $\bar{A}_0 = 1279.3$ spk/s and $|\bar{T}_6| < 10^{-10}$. (D) Left: Illustration of a random walk (cut for illustration purposes), overlaid onto the firing pattern of a single grid cell. Right: Population firing rate as a function of movement direction for random walks with $\bar{A}_0 = 1281.0$ spk/s and $|\bar{T}_6| = 6.7 \cdot 10^{-3}$. (E) Hexasymmetry (color coded) as a function of HD tuning width and alignment jitter for random-walk trajectories. Higher hexasymmetry values are achieved for stronger HD tuning and tighter alignment of the preferred head directions to the grid axes. The red symbols correspond to the three parameter combinations used in subplots (F–H) for further illustration. (F) Population firing rate as a function of movement direction for a random walk trajectory with jitter $\sigma_c = 0$ and concentration parameter $\kappa_c = 50$ rad⁻² (tuning width $\approx 8.1^\circ$). (G) Population firing rate as a function of movement direction for a random walk with jitter $\sigma_c = 1.5^\circ$ and concentration parameter $\kappa_c = 25$ rad⁻² (tuning width $\approx 11.5^\circ$). (H) Population firing rate as a function of movement direction for a random walk with jitter $\sigma_c = 3^\circ$ and concentration parameter $\kappa_c = 10$ rad⁻² (tuning width $\approx 18.1^\circ$). All simulations presented in this figure use $p_c = 100\%$ conjunctive ($N = 1024$) cells, which is higher than in empirical studies (Sargolini et al., 2006; Boccara et al., 2010). In subplots B–D and F–H, the black lines and light gray lines represent the results from the numerical simulations of Eq. (8) and the analytical derivation in Eq. (32), respectively. H, neural hexasymmetry; spk/s, spikes per second.

183 proposes that grid-cell activity is subject to firing-rate adaptation and thus leads to reduced grid-cell
184 activity when moving along the grid axes as compared to when moving along other directions than the
185 grid axes (Fig. 3A). This difference is due to the fact that the grid fields of fewer grid cells are traversed
186 relatively more often when the subjects moves along the grid axes (associated with strong repetition
187 suppression), whereas the grid fields of more grid cells are traversed relatively less often when moving
188 not along the grid axes (weak repetition suppression) (Doeller et al., 2010).

189 The repetition suppression hypothesis depends on two adaptation parameters: the adaptation time
190 constant τ_r and the adaptation weight w_r (Eq. 5). We found that the optimal adaptation time constant,
191 which leads to the largest hexasymmetry, is roughly the subject's speed v divided by the grid scale
192 s (Fig. 3B). Larger values of the adaptation weight generally resulted in larger hexasymmetry values
193 (Fig. 3B), but we ultimately constrained values of the adaptation weight to $0 \leq w_r < 1$, as negative values
194 would cause enhancement rather than suppression, and values larger than one would lead to suppression
195 that is stronger than the peak activity of the single grid cell (Fig. 3B). When examining how the different
196 types of navigation trajectories affected hexadirectional modulations based on repetition suppression, we
197 found that star-like and piece-wise linear walks resulted in clear and significant hexasymmetry values
198 (Fig. 3C, D), which is driven by the long linear segments in these trajectory types. In contrast, random
199 walks did not result in a significant hexadirectional modulation of sum grid-cell activity because the large
200 tortuosity of the random walk ($\sigma_\theta = 0.5 \text{ rad/s}^{1/2}$) basically removes the effects of repetition suppression.
201 Examining in detail which tortuosity values would still lead to some hexadirectional modulation due to
202 repetition suppression, we found that $\sigma_\theta \lesssim 0.25 \text{ rad/s}^{1/2}$ was the upper bound. For smaller values of the
203 tortuosity parameter trajectories are straight enough to allow for a hexadirectional modulation of sum
204 grid-cell activity (Fig. S2).

205 A notable difference of the repetition suppression hypothesis compared to the conjunctive grid by
206 head-direction cell hypothesis is that the apparent preferred grid orientation (i.e., the movement direc-
207 tions resulting in the highest sum grid-cell activity) is shifted by 30° and is thus exactly misaligned
208 with the grid axes of the individual grid cells (Fig. 3, C–D). This is due to the fact that the adaptation
209 mechanism suppresses grid-cell activity more strongly when moving aligned with a grid axis as compared
210 to when moving misaligned with a grid axis (Fig. 3A).

211 **2.2.3 Structure-function mapping hypothesis**

212 We next investigated the structure-function mapping hypothesis, according to which a hexadirectional
213 modulation of entorhinal cortex activity emerges in situations when a population of grid cells is recorded
214 whose grid phase offsets are biased towards a particular offset (Kunz et al., 2019). In the ideal case, all
215 grid phase offsets are identical (and thus all grid cells behave like a single grid cell). This hypothesis
216 is called “structure-function mapping hypothesis” because of a direct mapping between the anatomical
217 locations of the grid cells in the entorhinal cortex and their functional firing fields in space.

218 We found indeed that highly clustered grid phase offsets ($\kappa_s = 10$) resulted in significant hexadi-
219 rectional modulations of sum grid-cell activity when the subject performed star-like walks starting at a
220 phase offset of $(0, 0)$, i.e. the center of the cluster of firing fields of grid cells (Fig. 4A). Interestingly, we
221 observed that the hexasymmetry values during star-like walks were strongly dependent on the subject's
222 starting location relative to the locations of the grid fields: only particular starting locations such as $(0, 0)$
223 or $(0.3, 0.3)$ led to clear hexasymmetry whereas others, e.g. $(0.6, 0)$, did not (Fig. 4D, left). Additionally,
224 the “apparent preferred grid orientation” (i.e., the movement directions associated with the highest sum
225 grid-cell activity) was shifted by 30° for certain offsets in the unit rhombus illustrating the subject's
226 starting locations relative to the firing-field locations (Fig. 4D, right). It was furthermore notable that
227 the summed grid-cell activity as a function of movement direction did not show a sinusoidal modulation

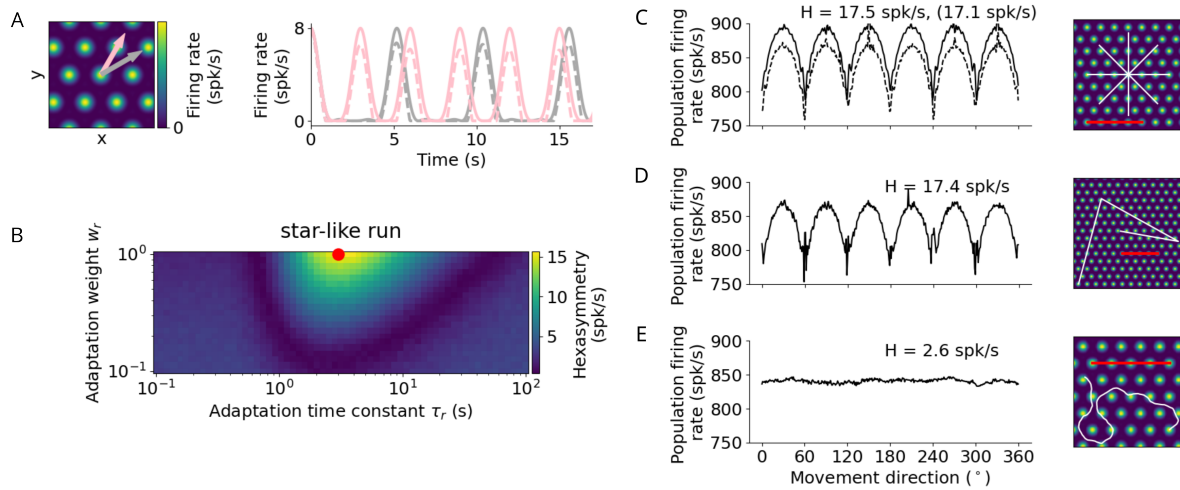


Figure 3: Repetition suppression hypothesis. (A) Left: Tuning of an example grid cell with aligned (pink arrow) and misaligned (gray arrow) movement directions. Right: Examples of firing-rate adaptation (dashed lines) for an aligned run (pink) and a misaligned run (gray). More firing-rate adaptation (i.e., stronger repetition suppression) occurs along the aligned run. For both runs, firing rates are reduced compared to the case without adaptation (solid lines). (B) Simulations of hexasymmetry as a function strength (w_r) and time constant (τ_r) of adaptation (averaged over 20 realisations of 1024 grid cells with phase offsets drawn from a uniform distribution on the unit rhombus) point to an optimal set of parameters for star-like runs. Red dot marks parameters used in (C–E). (C) Population firing rate as a function of the subject’s movement direction for a star-like run (at an offset of $(0, 0)$). The solid line represents a single run where adaptation does not carry over when sampling different movement directions (i.e., the “teleportation” between path segments resets the repetition suppression effects), and movement directions are sampled consecutively from 0° to 359° in steps of 1° (mean firing rate $\bar{A}_0 = 866.4$ spk/s, path hexasymmetry $|\bar{T}_6| < 10^{-10}$). The dashed line represents a single run with adaptation carry-over and randomly sampled movement directions without replacement ($\bar{A}_0 = 839.8$ spk/s, path hexasymmetry $|\bar{T}_6| < 10^{-10}$, the corresponding hexasymmetry is shown in brackets). (D) Population firing rate as a function of movement direction for a piecewise linear walk ($\bar{A}_0 = 839.0$ spk/s, $|\bar{T}_6| < 10^{-10}$). (E) Population firing rate as a function of movement direction for a random walk ($\bar{A}_0 = 839.7$ spk/s, $|\bar{T}_6| = 6.7 \cdot 10^{-3}$). spk/s, spikes per second. For all repetition-suppression simulations, the grid phase offsets were sampled randomly from a uniform distribution across the unit rhombus, and the hexasymmetries were averaged over 20 realisations of random grid phase offsets. The scale bars (red) in (C–E) represent a distance of 120 cm.

228 but rather exhibited relatively sharp peaks at multiples of 60° with additional small peaks in between
 229 (Fig. 4A, right). This pattern is clearly distinct from the more sinusoidal modulation of sum grid-cell
 230 activity resulting from the conjunctive grid by head-direction cell hypothesis (Fig. 2) and the repetition
 231 suppression hypothesis (Fig. 3).

232 When examining piecewise linear walks and random walks, hexasymmetry appeared to be consider-
 233 ably lower as compared to simulations with star-like walks (Fig. 4, B and C). For piecewise linear walks,
 234 population grid-cell activity as a function of movement direction again exhibited sharp, non-sinusoidal
 235 peaks at multiples of 60° , in both positive and negative directions (Fig. 4B). The hexasymmetry values
 236 furthermore exhibited large fluctuations and did not show a systematic dependency on the starting lo-
 237 cation of the subject’s navigation trajectory relative to the locations of the grid fields (Fig. 4, E and F,
 238 left), which is due to the fact that these navigation trajectories randomize the starting locations of all
 239 path segments. Accordingly, the apparent preferred grid orientations varied randomly as a function of
 240 the starting location of the very first path segment and did not exhibit systematic shifts (Fig. 4, E and
 241 F, right), which is in contrast to the clear shifts in the apparent preferred grid orientations for star-like
 242 walks (Fig. 4D).

243 In the above-mentioned simulations for the structure-function mapping hypothesis, we chose high
244 values for the clustering of the grid phase offsets from all grid cells. Specifically, we set the clustering
245 parameter to $\kappa_s = 10$, due to which the centers of the firing fields of different grid cells were very close
246 to each other (insets in Fig. 4, A–C, right). However, previous empirical studies (Gu et al., 2018; Heys
247 et al., 2014) showed that the clustering parameters are several orders of magnitude smaller than the
248 strong clustering we considered for our earlier simulations. These empirically determined parameters
249 are actually relatively close to randomly distributed grid phases (Fig. 4, G–Q), and simple clustering
250 is associated with a parameter $\kappa_s \approx 0.014$ (Fig. 4M). Clustering parameters were also low when we
251 implemented higher-order spatial clustering of grid phase offsets by adding some longer-range spatial
252 autocorrelations to the grid-phase offsets (Fig. 4, N–Q) (Gu et al., 2018), which led to a clustering
253 parameter $\kappa_s \approx 0.052$ (Fig. 4Q). Taken together, these more “realistic” clustering parameters result in
254 clearly reduced hexasymmetries, which is described below and summarized in Fig. 5.

255 Together, our results (Fig. 4A–C) indicate that for the structure-function mapping hypothesis the
256 navigation pattern has a strong influence on the measured neuronal hexasymmetry H . The hexasym-
257 metry was largest ($H = 59.7$ spk/s) for the star-like walk with specific starting locations [e.g., (0, 0)],
258 smaller ($H = 12.1$ spk/s) for piecewise linear walks, and smallest ($H = 8.0$ spk/s) for random walks.
259 Moreover, the absolute values of these hexasymmetries were quite low compared to the average firing
260 rate of about 1024 spk/s of the simulated population of grid cells ($N = 1024$, each having an average
261 firing rate of 1 spk/s). We thus wondered whether the hexasymmetries of the associated navigation paths
262 substantially contributed to the neuronal hexasymmetries H .

263 In line with this idea, we found that the path hexasymmetries for random walks was proportional to
264 $1/\sqrt{M}$ for a large number M of steps (Figure S1). We thus examined neural hexasymmetries H across a
265 broad range of total trajectory distances (using piecewise linear walks) and observed that H decreased also
266 as $1/\sqrt{M}$ (Fig. 4T). This led us to conclude that the apparent neural hexasymmetry H of summed grid-
267 cell activity for piecewise linear walks was driven by random subsamples of all path segments—specifically
268 those path segments crossing through grid fields. These subsamples of path segments necessarily exhibit
269 higher path hexasymmetries than the full set of path segments that has basically zero path hexasymmetry
270 by construction (Fig. S4). Critically, we thus conclude that, for piecewise linear walks, hexasymmetry
271 values were driven by a subsampling of the movement directions due to the sparsity of the grid-field
272 locations. Similarly, for a random walk with tortuosity $\sigma_\theta = 0.5$ rad/s^{1/2}, we derived from Figure S1
273 that the expected path hexasymmetry for 9000 s simulation time ($M = 0.9 \cdot 10^6$ steps for $\Delta t = 0.01$ s) is
274 about 0.007, which results in a contribution to the neural hexasymmetry of $H \approx 7$ spk/s for a population
275 rate of about 1024 spk/s. This number is similar in magnitude to the obtained neural hexasymmetry
276 ($H = 8.0$ spk/s) in Fig. 4C and in Fig. 5; see also Fig. S4. We thus conclude that also for random walks
277 the hexasymmetry H obtained in the structure-function mapping case is mainly determined by the path
278 hexasymmetry.

279 Taken together, the structure-function mapping hypothesis with strong clustering can produce hex-
280 asymmetry values that are larger than expected from path hexasymmetries only with respect to star-like
281 walks, including a strong dependence on the subject’s starting location (Fig. 4D, left). This range of
282 values is comparable to those of the repetition-suppression hypothesis (Fig. 3), but values are at least
283 an order of magnitude smaller than in the conjunctive grid by head-direction cell case (Fig. 2).

284 **2.3 Overall evaluation of the three hypotheses**

285 To provide a systematic evaluation of the three hypotheses, we computed 300 realizations of each hy-
286 pothesis (using the simulated activity of 1024 cells), separately for each type of navigation and for both
287 ideal and more realistic parameter settings (Fig. 5). This resulted in 18 different hypothesis condi-

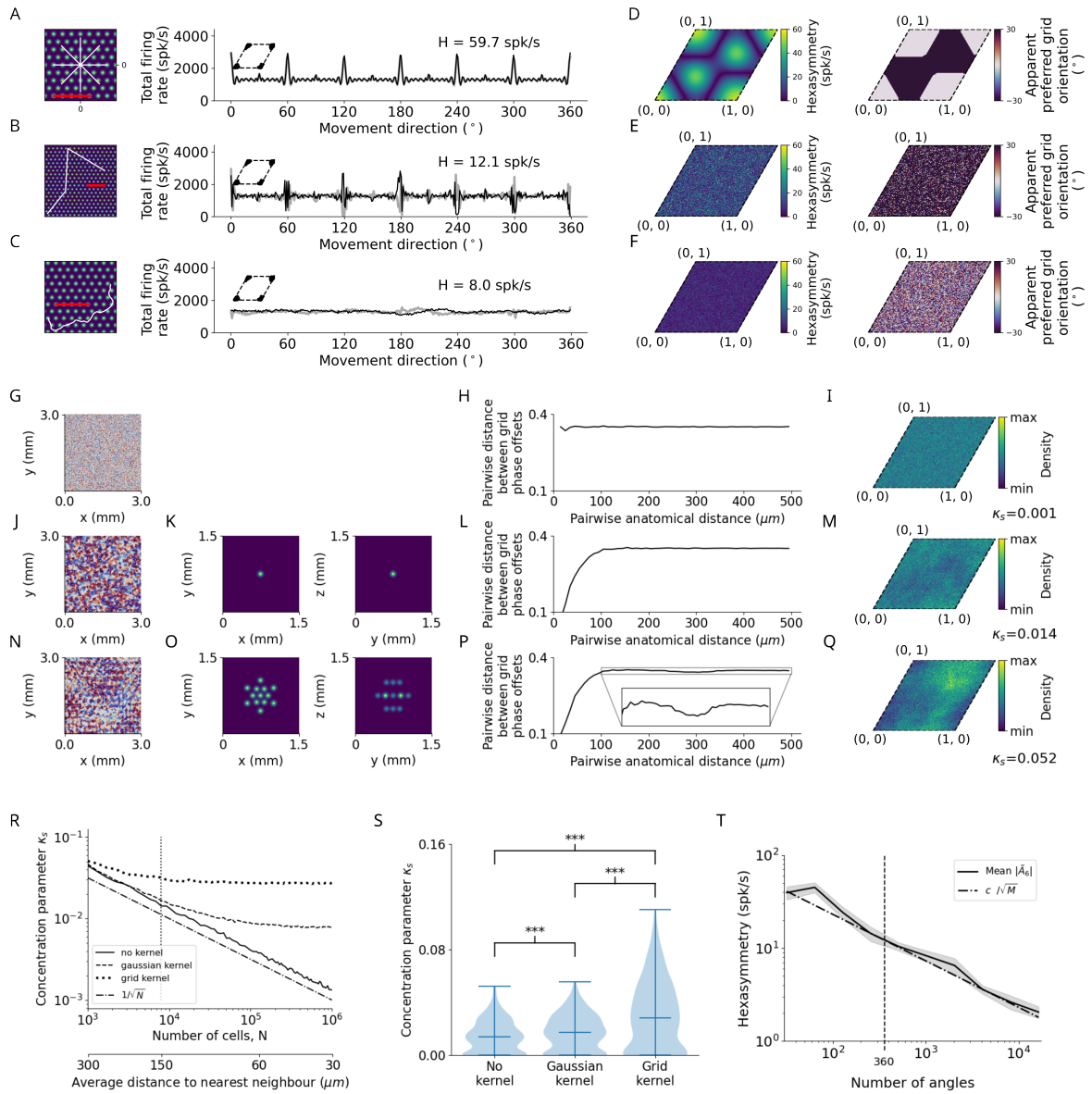


Figure 4: Structure-function mapping hypothesis. (A–C) Left: Short example trajectories (white) overlaid onto the firing-rate pattern of an example grid cell (colored). Shown trajectories are for illustration purposes only, and do not reflect the full length of the simulation. The scale bars (red) represent a distance of 120 cm. Right: Population firing rate as a function of the movement direction. Black and light gray lines represent the results from the numerical simulations of Eq. (8) and the analytical derivation in Eq. (32), respectively. Grid phase offsets cells are strongly clustered at (0,0) with $\kappa_s = 10$ (left inset). (A) Left: Subsegment of a star-like walk. Right: Population firing rate as a function of the movement direction for star-like runs originating at phase offset (0,0) with mean firing rate $\bar{A}_0 = 1362.4$ spk/s (spikes/second) and path hexasymmetry $|\tilde{T}_6| < 10^{-10}$. The grid phase offsets of the grid cells are also clustered at (0,0) (left inset). (B) Left: Subsegment of a piece-wise linear walk. Right: Population firing rate as a function of the movement direction for a piece-wise linear trajectory. $\bar{A}_0 = 1244.3$ spk/s, $|\tilde{T}_6| < 10^{-10}$. (C) Left: Subsegment of a random walk. Right: Population firing rate as a function of movement direction for a random walk. $\bar{A}_0 = 1305.4$ spk/s, $|\tilde{T}_6| = 6.7 \cdot 10^{-3}$ spk/s. (D) Left: Hexasymmetry as a function of the subject’s starting location (relative to grid phase offset). Right: Movement direction associated with the highest sum grid-cell activity, i.e. the phase of peaks in (A, right), has a bimodal distribution (0 or 30°).

(E) Same as (D) but for piecewise linear walks. (F) Same as (D) but for random walks. (G) Example of a two-dimensional slice of a three-dimensional (3D) random-field simulation with a spatial resolution of $15 \mu\text{m}$. The simulated volume of $(3 \times 3 \times 3) \text{ mm}^3$ represents the approximate spatial extent of a voxel in fMRI experiments. (H) The pairwise phase distance in the rhombus is shown as a function of the pairwise anatomical distance for all pairs of simulated cells from (G). Since no spatial correlation structure is induced, the pairwise phase distance between grid cells remains constant when varying the pairwise anatomical distance between them. (I) The resulting phase clustering for 200^3 simulated grid cells in a $(3 \times 3 \times 3) \text{ mm}^3$ voxel. Brighter colors indicate a higher prevalence of a particular grid phase offset. The distribution of grid phases appears to be homogeneous with a clustering concentration parameter of $\kappa_s = 0.001$. (J–M) Same as (G–I) but for a convolution of the 3D random field with the 3D Gaussian correlation kernel of width $30 \mu\text{m}$ shown in (K). Grid cells located next to each other in anatomical space ($\lesssim 30 \mu\text{m}$) exhibit similar grid phase offsets (L). No clear clustering is visible for a clustering concentration parameter of $\kappa_s = 0.014$ (M). (N–Q) Same as (J–M) but for the grid-like correlation kernel shown in (O), which adds some longer-range spatial autocorrelation to the grid phase offsets of different grid cells. The pairwise phase distance (P) exhibits a dip around $300 \mu\text{m}$. Note in (Q) that the prevalence of particular grid phase offsets is more biased than in (M), with a clustering concentration parameter of $\kappa_s = 0.052$. (R) Dependence of the clustering concentration parameter κ_s on the number N of grid cells in a voxel. A random distribution of grid cells in anatomical space was obtained by subsampling from the 200^3 grid cells simulated in (G–Q) over 300 realizations. We found $\kappa_s \approx 0.05$ for 10^3 grid cells in a voxel, and that κ_s decreases monotonically as N is increased. Convolution of grid phase offsets with a correlation kernel (as in J–Q) leads to saturation of κ_s for large N . Note that the range of values of κ_s here is three orders of magnitude smaller than the strong clustering considered in (A–C). The dashed-dotted line depicts the line $1/\sqrt{N}$ for comparison. The vertical dotted line at $N = 20^3$ corresponds to the empirically estimated count of grid cells in a $(3 \times 3 \times 3) \text{ mm}^3$ fMRI voxel. The secondary lower horizontal axis shows the average distance between uniformly distributed grid cells in anatomical space. (S) The distribution of the clustering concentration parameter κ_s when using either no kernel, a Gaussian kernel, or a grid-like kernel for 20^3 grid cells subsampled from the 200^3 grid cells simulated in (G–Q) over 300 realizations. While the grid-like kernel results in a larger maximum value of the clustering concentration parameter, a large number of realizations results in relatively low clustering. (T) The dependence of the hexasymmetry on the number of angles sampled when unwrapping the star for the piece-wise linear walk, averaged over 20 trajectories for each data point. Each additional angle sampled adds 300 cm to the total length of the path. A line proportional to c/\sqrt{M} is plotted for comparison, where c is an offset parameter ($c = 4000 \text{ spk/s}$) chosen such that the slope of $|\tilde{A}_6|$ can be compared to the slope of $1/\sqrt{M}$. The close fit between the solid and dashed lines indicates that the neural hexasymmetry $|\tilde{A}_6|$ is highly correlated with the path hexasymmetry $|\tilde{T}_6|$. The vertical dotted line at 360 sampled angles corresponds to the number of angles sampled in the star-like run and the piece-wise linear run for all main figures.

288 tions. For each hypothesis condition, we assessed its statistical significance by performing nonparametric
289 Mann-Whitney U tests between the neural hexasymmetries ($H := |\tilde{A}_6|$; see also Eq. 12) and the product
290 $|\tilde{T}_6| \cdot \tilde{A}_0$ with the multipliers path hexasymmetry $|\tilde{T}_6|$ and average population activity \tilde{A}_0 .

291 For the conjunctive hypothesis, we found that all three types of navigation led to significant neural
292 hexasymmetries. This was the case for both ideal parameters (Mann-Whitney U tests, all $U = 0$, all
293 $P < 0.001$) and for more realistic parameters (Mann-Whitney U tests, all $U = 0$, all $P < 0.001$). We
294 derived the more realistic parameters from a previous study (Doeller et al., 2010). For star-like walks and
295 piecewise linear walks, the path hexasymmetries multiplied with the average population activities were
296 near zero because we designed these navigation paths to equally cover all different movement directions.
297 For random walks, the path hexasymmetries multiplied with the average population activities were at
298 values of about 7 spikes per second and showed larger variability because the directions of the random
299 walks were not predefined and could thus vary with regard to their hexasymmetries. If the conjunctive
300 hypothesis was true, fMRI studies should thus see a hexadirectional modulation of entorhinal fMRI
301 activity irrespective of the exact type of the subjects' navigation paths.

302 For the repetition suppression hypothesis, we found that star-like walks and piecewise linear walks

303 resulted in significant neural hexasymmetries for both ideal and weaker parameters (Mann-Whitney U
304 tests, all $U = 0$, all $P < 0.001$), whereas random walks did not (Mann-Whitney U tests, both $U > 1753$,
305 both $P > 0.405$). We obtained the weaker, more realistic parameters by dividing the ideal parameters by
306 2 because we were not aware of empirical investigations regarding repetition-suppression effects in single
307 grid cells. For random walks, the path hexasymmetries multiplied with the average population activities
308 were lower as compared to the other two hypotheses because the repetition suppression necessarily leads
309 to lower average population activities. If the repetition suppression hypothesis was true, fMRI studies
310 should thus observe significant neural hexasymmetries only for star-like walks and piecewise linear walks,
311 whereas random walks (with large enough tortuosities, Fig. S2) should not lead to significant neural
312 hexasymmetries.

313 Regarding the structure-function mapping hypothesis, the statistical tests showed that most of the
314 hypothesis conditions resulted in significant neural hexasymmetries as compared to the path hexasym-
315 metries multiplied with the average population activities. This was the case for both ideal parameters
316 (Mann-Whitney U tests, all $U < 736$, all $P < 0.001$) and more realistic parameters (Mann-Whitney U
317 tests for star-like walks and piecewise linear walks, all $U = 0$, all $P < 0.001$). We derived the more
318 realistic parameters from a previous study (Gu et al., 2018). Only the hypothesis condition with random
319 walks and more realistic parameters exhibited no significant neural hexasymmetries (Mann-Whitney U
320 test, $U = 1786$, $P = 0.472$). However, these results regarding the structure-function mapping hypothesis
321 should be treated with great caution. Firstly, the neural hexasymmetries for star-like walks heavily
322 depend on the starting location of the subject relative to the grid fields, and different starting locations
323 lead to different apparent grid orientations (Fig. 4D). Secondly, the significant results for the navigation
324 conditions with piecewise linear walks and random walks actually result from an inhomogeneous sampling
325 of movement directions through the grid fields and therefore do not reflect true neural hexasymmetries
326 (Fig. 4T). Only the structure-function mapping hypothesis is susceptible to this effect because the grid
327 fields are clustered at similar spatial locations (whereas the grid fields are homogeneously distributed
328 in the case of the conjunctive hypothesis and the repetition suppression hypothesis). In simulations
329 with infinitely long paths, the neural hexasymmetries (for the navigation types of piecewise linear walks
330 and random walks) would not be significantly higher than the path hexasymmetries multiplied with
331 the average population activities. In empirical studies, this effect can be detected by correlating the
332 subject-specific path distances with the subject-specific neural hexasymmetries: if there is a generally
333 negative relationship, this will hint at the fact that the neural hexasymmetries are basically due to rel-
334 evant path hexasymmetries of path segments crossing the grid fields. In essence, we therefore believe
335 that the structure-function mapping hypothesis leads to true neural hexasymmetry only in the case of
336 star-like walks.

337 **2.4 Influence of other factors**

338 Our simulations above were performed in an infinite spatial environment, which is different from empirical
339 studies in which subjects navigate finite environments. We were thus curious whether the size and shape
340 of finite environments could affect the strength of hexadirectional modulations of population grid-cell
341 activity.

342 Our simulations showed that for both circular and square environments, hexasymmetry strengths
343 did not considerably depend on the size of the environment when the subject performed random walks
344 (Fig. S5). Similarly, rotating the navigation trajectories relative to the grid patterns did not affect the
345 hexasymmetry strengths (Fig. S6). These results thus suggest that experiments in animals and humans
346 can use various types and sizes of the environments to investigate hexadirectional modulations of sum
347 grid-cell activity.

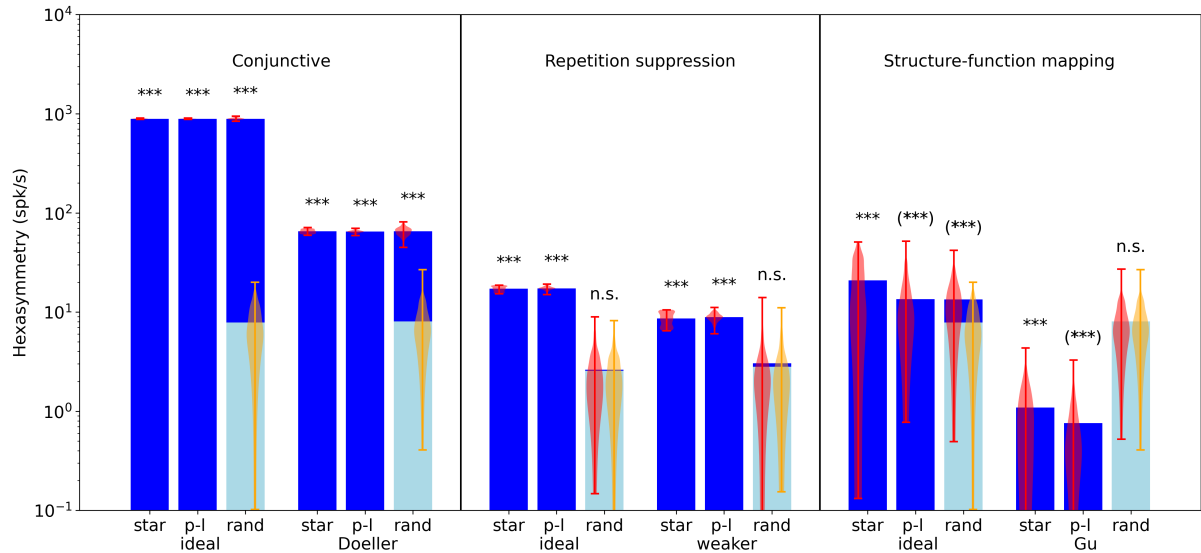


Figure 5: Comparison of hexasymmetry resulting from the three hypotheses. Each of the three hypotheses is implemented for three different types of navigation trajectories: star-like walks (“star”), piece-wise linear random walks (“p-l”), and random walks with small step size (“rand”). For each setting, we show the average hexasymmetry $|\tilde{A}_6|$ for 1024 cells (dark blue bars) and the average contribution of the trajectory $|T_6| \cdot \tilde{A}_0$ (light blue bars) where \tilde{A}_0 is the (variable) average population activity; see Methods for definitions of symbols. The violin plots depict the distributions for firing-rate hexasymmetry (red) and path hexasymmetry (orange). For each hypothesis, we calculate the hexasymmetry for “ideal” parameters (conjunctive: $p_c = 1$, $\kappa_c = 50 \text{ rad}^{-2}$, $\sigma_c = 0$; repetition suppression: $\tau_r = 3 \text{ s}$, $w_r = 1$; clustering: $\kappa_s = 10$) as well as more realistic parameters [conjunctive “Doeller”: $p_c = 0.33$, $\kappa_c = 10 \text{ rad}^{-2}$, $\sigma_c = 3^\circ$ motivated by (Doeller et al., 2010; Boccarda et al., 2010; Sargolini et al., 2006); repetition suppression “weaker”: $\tau_r = 1.5 \text{ s}$, $w_r = 0.5$; clustering “Gu”: $\kappa_s = 0.1$ motivated by (Gu et al., 2018)]. The parameters for the random-walk scenario are $T = 9000 \text{ s}$ and $\Delta t = 0.01 \text{ s}$; see Table 1 for a description of parameters. Each hypothesis condition was simulated for 300 realizations. ***, $P < 0.001$; n.s., not significant; (***) , a seemingly significant result ($P < 0.001$) that is thought to be spurious (see Results section). For pair-wise comparisons of the hexasymmetry values from different trajectory types for each set of parameters, see Fig. S3.

3 Discussion

We performed numerical simulations and analytical estimations to examine how the activity of grid cells could potentially lead to a neural population signal in the entorhinal cortex. Such a neural population signal has been observed in multiple fMRI studies (Doeller et al., 2010; Kunz et al., 2015; Constantinescu et al., 2016; Horner et al., 2016; Bellmund et al., 2016; Stangl et al., 2018; Nau et al., 2018; Julian et al., 2018; Bierbrauer et al., 2020; Julian and Doeller, 2021; Bongioanni et al., 2021; Moon et al., 2022) and iEEG/MEG studies (Maidenbaum et al., 2018; Chen et al., 2018; Staudigl et al., 2018; Chen et al., 2021; Wang and Wang, 2021), and consists of a hexadirectional modulation of the entorhinal fMRI/iEEG signal as a function of the subject’s movement direction through its spatial environment. We examined three hypotheses that have been previously suggested as potential mechanisms underlying the emergence of the hexadirectional population signal in the entorhinal cortex (Doeller et al., 2010; Kunz et al., 2019) and found that all three hypotheses can—in principle and in ideal situations—lead to a hexadirectional modulation of entorhinal cortex population activity.

A major observation of this study is that the way how subjects navigate through the environment has a major influence on whether a hexadirectional population signal can be observed. We distinguished three major types of navigation: navigation with random walk trajectories in which straight paths are quite short and resemble the navigation pattern in rodents; navigation with piecewise linear trajectories

365 in which the subject navigates along straight paths combined with random sharp turns between the
366 straight segments; and navigation with star-like trajectories, in which the subject starts each path from
367 a fixed center location and navigates along a straight path with a predetermined allocentric direction
368 and distance. Critically, we found that the conjunctive hypothesis leads to a hexadirectional population
369 signal irrespective of the specific type of navigation; that the repetition suppression hypothesis leads to
370 hexadirectional population signals only in the case of star-like trajectories and piecewise linear trajec-
371 tories (but not for random trajectories); and that for the structure-function mapping hypothesis “true”
372 hexadirectional population signals can only be observed for star-like trajectories.

373 The observation that the type of navigation paths influences whether a hypothesis can lead to hexadi-
374 rectional population signals of the entorhinal cortex is informative to future fMRI/iEEG studies, which
375 could empirically evaluate which of the three hypotheses is most likely to be true: By asking or requiring
376 the subjects to navigate in different ways through the task environments (in a star-like fashion, in a
377 piecewise linear fashion, and in a random fashion), these future fMRI/iEEG studies could demonstrate
378 whether hexadirectional population signals are present in all three navigation conditions (speaking in
379 favor of the conjunctive hypothesis); whether they are present only during star-like or piecewise linear
380 trajectories (in favor of the repetition suppression hypothesis); or whether they are mainly visible for
381 star-like trajectories and exhibit a systematic decrease with increasing trajectory length for piecewise
382 linear and random walks (in this case speaking in favor of the structure-function mapping hypothesis).
383 In contrast to this major effect of navigation type on the presence of hexadirectional signals, the size
384 and shape of the environment did not influence the strength of the hexadirectional signals in a relevant
385 manner (Figs. S5 and S6).

386 Another insight of this study is that the exact biological properties of grid cells play a major role
387 regarding the question whether hexadirectional population signals can be observed. For example, the
388 conjunctive hypothesis cannot lead to hexadirectional population signals if the tuning width of the
389 conjunctive grid by head-direction cells is too broad or if the preferred directions of the conjunctive
390 cells are not precisely aligned with the grid axes of the grid cells. The structure-function mapping
391 hypothesis heavily relies on the property of neighboring grid cells to share a similar grid phase offset
392 (i.e., a high spatial autocorrelation of grid phases) and whether there might be longer-range spatial
393 autocorrelations between the grid phases (Gu et al., 2018). Whereas it currently seems possible that
394 grid cells and conjunctive grid by head-direction cells meet the necessary biological properties for the
395 conjunctive hypothesis (Doeller et al., 2010), it seems unlikely to us that the grid phases are clustered
396 strongly enough to facilitate a hexadirectional population signal. Regarding the repetition suppression
397 hypothesis, we are currently not aware of detailed measurements of the relevant grid-cell properties (i.e.,
398 the adaptation time constant τ_r and the adaptation weight w_r) so that it remains unclear to us to what
399 extent the repetition suppression hypothesis is biologically plausible. Future studies may thus quantify
400 the relevant properties of (human) grid cells in greater depth in order to help clarify which hypothesis
401 regarding the emergence of hexadirectional population signals may most likely be true.

402 A topic that this study did not investigate is the question of how the sum signal of single neurons
403 translates into fMRI and iEEG signals. In neocortical regions such as the auditory cortex, a clear linear
404 relationship between single-neuron activity and fMRI activity has been observed (Mukamel et al., 2005),
405 but it remains elusive whether this linear relationship also applies to the entorhinal cortex in general
406 and to entorhinal grid cells in particular. In the neighboring hippocampus, for example, the relationship
407 between single-neuron activity and the fMRI signal is highly complex (Ekstrom, 2010; Kunz et al., 2019).
408 Future studies are needed to detail the relationship between single-neuron firing and fMRI/iEEG signals
409 in the entorhinal cortex. This would allow us to clarify whether a hexadirectional modulation of sum
410 grid-cell activity directly results in a hexadirectional modulation of fMRI/iEEG activity or whether
411 currently unknown factors modulate the expression of hexadirectional fMRI/iEEG signals.

412 4 Conclusion

413 Using numerical simulations and analytical derivations we showed that a hexadirectional neural pop-
414 ulation signal can emerge from the activity of grid cells given the ideal conditions of three different
415 hypotheses. Whether a given hypothesis leads to a hexadirectional population signal is significantly in-
416 fluenced by the subjects' type of navigation through the spatial environment and by the exact biological
417 properties of human grid cells.

418 5 Methods

419 5.1 Trajectory modeling

420 To describe grid-cell activity as a function of time t during which a subject (animal or human) is
421 exploring an environment, we model three distinct trajectory types. We first describe trajectory types in
422 environments without bounds, which are quasi infinite, and then add rules that account for boundaries.

423 5.1.1 Environments without boundaries

424 The first trajectory type is a random walk $X_t = [x_t, y_t]$, which is defined by

$$\frac{dX_t}{dt} = v [\cos(\theta_t), \sin(\theta_t)] \quad (1)$$

425 with $\theta_t = \sigma_\theta \cdot W_t$ where σ_θ controls the tortuosity of the trajectory and W_t is a standard Wiener
426 process. In a numerical simulation with a time step Δt , the angle is updated in each time step by
427 $\theta_{t+\Delta t} = \theta_t + \sigma_\theta \cdot \Delta W$ where ΔW is a normally distributed random variable with variance Δt . The
428 variable v depicts the (constant) speed.

429 The second type of navigation is a star-like walk, where the subject moves radially outwards from
430 a predefined origin in space at a certain angle θ on a straight line to a maximum distance r_{max} at a
431 constant speed v . In simulations, this movement is repeated (with the same predefined origin) for N_θ
432 angles that are equally spaced on the interval $[0, 2\pi)$. Within each individual radial path, the subject
433 does not turn around and move back to the origin, i.e., the entire trajectory of N_θ radial paths is not
434 continuous.

435 Finally, we introduce a piecewise linear walk, which is constructed by placing all the radial paths of
436 the star-like walk end-to-end such that they form one single continuous trajectory of length $N_\theta r_{max}$. The
437 trajectory thus consists of successive straight runs for the simulated subject, which can be interpreted
438 as a random walk with a time step $\Delta t = r_{max}/v$ and directions that are sampled uniformly without
439 replacement from a predetermined set of angles. In comparison to the random walk and the star-like
440 walk, this procedure presumably reflects the situation in human virtual-reality setups most closely, as
441 participants often move along straight trajectories with intermittent turns (Doeller et al., 2010; Kunz
442 et al., 2015; Horner et al., 2016).

443 5.1.2 Environments with boundaries

444 Most virtual-reality studies in humans use finite instead of infinite spatial environments to examine grid-
445 like representations. We wondered whether the size and the shape of these finite environments might
446 modulate the strength of macroscopic grid-like representations obtained through one or more of the three
447 hypotheses. Hence, we performed our simulations not only in infinite but also in finite environments with
448 a given size (between one and six times the grid spacing) and shape (circle and square).

449 For random-walk trajectories, we enforce that the navigating subject stays within the circular or
 450 square environment by performing an “out-of-bounds check” at each time point. This means that,
 451 after every time step Δt , we measure the distance that the subject has moved outside of the boundary.
 452 This is done differently in square and circular environments, both of which are centered at the origin
 453 ($x = 0, y = 0$). In the square environment, we define the variables Δx and Δy as the distance the
 454 subject has moved out of bounds in the x and y coordinates, respectively. Let L be the half of the
 455 length of its sides. Δx and Δy are then defined as $\Delta x = \max[|x| - L, 0]$ and $\Delta y = \max[|y| - L, 0]$. For
 456 circular environments, let R be the radius of the circle, and let $\vec{r} = (x, y)$ be the position vector of the
 457 subject. We then introduce the measure $\Delta r := \max[|\vec{r}| - R, 0]$, such that Δr is non-zero only when
 458 the subject has moved outside of the circular boundary. If at any time point either Δx , Δy , or Δr are
 459 non-zero, the out-of-bounds check fails. In this case, we reject the movement in this time step and keep
 460 resampling a new angle θ_t (Kropff and Treves, 2008; Si et al., 2012) until the check succeeds, meaning
 461 that the subject has made a move that is within the boundaries of the environment. If Δx , Δy , or Δr
 462 remain non-zero for 50 consecutive samples of θ_t , we temporarily increase the tortuosity σ_θ by a factor
 463 1.1. Without this increase in tortuosity, the subject tends to get stuck when approaching the boundary
 464 at angles close to the perpendicular or at the corners of the square boundary. The tortuosity is reset
 465 to its initial value once a valid move is made. We visually checked the random-walk trajectories, which
 466 show some oversampling along the boundaries, and found that they were comparable to the navigation
 467 trajectories in rodent studies (e.g. Hafting et al., 2005).

468 5.2 Implementation of grid cell activity

469 The activity profile G_i of grid cell i (for $i = 1, \dots, N$ in a population of N grid cells) is modelled as the
 470 product of three cosine waves rotated by 60° ($= \pi/3$) from each other:

$$G_i(x, y) = \frac{A_{\max}}{8} \prod_{k=0}^2 \left(1 + \cos \left[\frac{4\pi}{\sqrt{3}s_i} \sin \left(\frac{\pi}{3}k + \gamma_i \right) (x - s_i x_{\text{off},i}) + \frac{4\pi}{\sqrt{3}s_i} \cos \left(\frac{\pi}{3}k + \gamma_i \right) (y - s_i y_{\text{off},i}) \right] \right) \quad (2)$$

471 where A_{\max} is the grid cell’s maximal firing rate, s_i depicts the cell’s grid spatial scale (“grid spacing”),
 472 $x_{\text{off},i}$ and $y_{\text{off},i}$ are the phase offsets of the grid (“grid phase”) in the two spatial dimensions (called x
 473 and y here), and γ_i is the orientation of the grid (“grid orientation”); see Table 1 for numerical values of
 474 parameters and Fig. 1A for an illustration of the three grid characteristics.

475 To describe the activity of many grid cells (for example in a voxel for an MRI scan), we sum up the
 476 firing rates of N grid cells in Eq. (2). For a given trajectory $X_t = [x_t, y_t]$, the macroscopic activity as a
 477 function of time t is then simply described by the sum $\sum_{i=1}^N G_i(x_t, y_t)$.

478 5.3 Implementation of the three hypotheses to explain macroscopic grid-like 479 representations

480 Here we summarize how the activity in a population of N grid cells can be described if they also exhibit
 481 (i) head-direction tuning, (ii) repetition suppression (i.e., firing-rate adaptation), or (iii) grid phases that
 482 are clustered across grid cells.

483 In all our models, the activity G_i of a grid cell is described by Eq. (2). Different grid cells typically
 484 have different phase offsets ($x_{\text{off},i}$, $y_{\text{off},i}$) but the same grid spacing $s_i := s$, $\forall i$ and grid orientation
 485 $\gamma_i := \gamma$, $\forall i$ (Hafting et al., 2005; Boccara et al., 2010; Gardner et al., 2022).

5.3.1 Conjunctive grid by head-direction cell hypothesis

To include head-direction tuning in our model, we note that a given trajectory X_t has an angle θ_t at time t . The summed firing rate, i.e. the population activity, A^c from N such conjunctive cells can then be described by

$$A^c(t) = \sum_{i=1}^N G_i(x_t, y_t) h_i(\theta_t) \quad (3)$$

where the upper index ‘c’ indicates “conjunctive” and where we incorporate conjunctive grid-head direction (HD) tuning via the (scaled by factor 2π) von-Mises distribution

$$h(\theta) = \frac{1}{I(\kappa_c)} \exp(\kappa_c \cos(\theta - \mu_c)) \quad (4)$$

with concentration parameter κ_c and preferred angle μ_c . The symbol I represents the modified Bessel function of the first kind of order 0. The parameter κ_c describes the width of the HD tuning: if $\kappa_c \rightarrow \infty$, the HD tuning is sharpest; the smaller κ_c , the wider the HD tuning (see Fig. 2); for $\kappa_c = 0$, there is no HD tuning, and our scaling leads to $h(\theta) \equiv 1$. We choose the preferred angle as $\mu_c = \frac{\pi}{3}k + \eta$ where k is randomly drawn from $\{0, 1, 2, 3, 4, 5\}$ and η is randomly drawn from a normal distribution with mean 0 and standard deviation σ_c . For $\sigma_c = 0$, the directional tuning is thus centered around a multiple of 60° . The parameter σ_c introduces jitter in the alignment of directional tuning to one of the grid axes.

We modelled the cases in which all grid cells show HD tuning (“ideal” case, fraction of conjunctive cells: $p_c = 1$) as well as a more “realistic” case in which only a third of the cells is conjunctive ($p_c = 1/3$; (Boccaro et al., 2010; Sargolini et al., 2006)). We note that this is an approximation, since the proportion of conjunctive cells is highly variable across layers of the entorhinal cortex, with up to 90% conjunctive cells in layer V.

5.3.2 Repetition suppression hypothesis

To incorporate repetition suppression in the model, we add an explicit dependence of grid-cell activity on time t . Specifically, we subject the firing rate G_i of a grid cell to an adaptation mechanism:

$$\begin{aligned} G_i^r(x_t, y_t, t) &= \max[G_i(x_t, y_t) - w_r a(t), 0] \\ \tau_r \frac{da}{dt} &= G_i(x_t, y_t, t) - a(t), \end{aligned} \quad (5)$$

where a depicts the adaptation variable, and τ_r and w_r are the repetition-suppression time constant and the weight of the suppression, respectively. The upper index ‘r’ in G_i^r indicates “repetition suppression”. The adaptation time constant τ_r is usually on the order of seconds, and the adaptation weight w_r is restricted to the interval $[0, 1]$. The maximum operation ‘ $\max(x)$ ’ in Eq. (5) ensures that the output firing rate G_i^r is always positive. Together, the summed firing rate A^r from N such adapting cells can then be described by

$$A^r(t) = \sum_{i=1}^N G_i^r(x_t, y_t, t). \quad (6)$$

We note that the explicit dependence of the firing rate G_i^r of grid cell i on time t needs to be considered separately for every cell for repetition suppression, which makes numerical simulations more computationally expensive. In contrast, the functions G_i (in Eq. (3)) and h_i (in Eq. (4)) for the conjunctive hypothesis depend also on time but only implicitly via the location $[x_t, y_t]$ and the direction θ_t of move-

517 ment at time t — and therefore the explicit time dependence of individual cells can be disregarded, which
 518 makes numerical simulations computationally cheaper.

519 5.3.3 Structure-function mapping hypothesis

520 The structure-function mapping hypothesis relies on a preferred grid phase for neighboring cells. We
 521 use two possible choices for the set of grid phases $(x_{\text{off},i}, y_{\text{off},i})$: they are either randomly uniformly
 522 distributed or clustered. For clustered spatial phases, we draw $x_{\text{off},i}$ and $y_{\text{off},i}$ independently, each from
 523 a univariate von-Mises distribution (with a defined central phase μ_s and concentration parameter κ_s).
 524 For a uniform distribution of grid phases, we note that even random fluctuations can lead to a certain
 525 degree of clustering of the grid-phase sample. We can describe the resulting summed activity of N grid
 526 cells simply by

$$A^s(t) = \sum_{i=1}^N G_i(x_t, y_t) \quad (7)$$

527 with the upper index ‘s’ representing “structure-function”.

528 5.4 Quantification of hexasymmetry of neural activity and trajectories

529 Combining the mathematical descriptions of grid cell activity for the three hypotheses (“conjunctive”,
 530 “repetition suppression”, and “structure-function”), we can denote the resulting population activity A
 531 of N grid cells by

$$A(t) = \sum_{i=1}^N G_i^r(x_t, y_t, t) h_i(\theta_t) \quad (8)$$

532 where $A_i(t) := G_i^r(x_t, y_t, t) h_i(\theta_t)$ is the firing rate of cell i . To derive from A the activity as a function of
 533 movement (or heading) direction θ_t , we focus on time steps of length Δt in which the trajectory is linear.
 534 In time step m , i.e., for time t in the time interval $[t_m, t_{m+1})$ where $t_m = m\Delta t$ and m is an integer, the
 535 trajectory has the fixed angle θ_m . The time-discrete mean activity $\bar{A}(t_m)$ associated to this interval is
 536 the average of $A(t)$ along the linear segment of the trajectory:

$$\bar{A}(t_m) = \frac{1}{\Delta t} \int_{t_m}^{t_{m+1}} dt \sum_{i=1}^N G_i^r(x_t, y_t, t) h_i(\theta_m) = \sum_{i=1}^N h_i(\theta_m) \frac{1}{\Delta t} \int_{t_m}^{t_{m+1}} dt G_i^r(x_t, y_t, t). \quad (9)$$

537 The integral in Eq. (9) is either calculated analytically, as derived in the following section, or numerically.
 538 For a total number of M time steps in a trajectory, the (normalized) mean activity $\tilde{A}(\phi)$ as a function
 539 of some head direction ϕ is then

$$\tilde{A}(\phi) = \frac{1}{M} \sum_{m=0}^{M-1} \delta(\phi - \theta_m) \bar{A}(t_m). \quad (10)$$

540 where δ is the Dirac delta distribution. With complex Fourier coefficients c_n (with $n \in \mathbb{N}$) defined as

$$c_n = \int_0^{2\pi} d\phi c(\phi) \exp(-nj\phi) \quad (11)$$

541 we can quantify the hexasymmetry H of the activity of a population of grid cells as

$$H := \left| \tilde{A}_6 \right| \stackrel{(11)}{=} \int_0^{2\pi} d\phi \tilde{A}(\phi) \exp(-6j\phi) \stackrel{(10)}{=} \left| \frac{1}{M} \sum_{m=0}^{M-1} \bar{A}(t_m) \exp(-6j\theta_m) \right| = \left| \sum_{i=1}^N \tilde{A}_{i6} \right| \quad (12)$$

542 where \tilde{A}_{i6} is the 6th Fourier coefficient of cell i . Furthermore, the average (over time) population activity
543 can be expressed as

$$\tilde{A}_0 = \frac{1}{M} \sum_{m=0}^{M-1} \bar{A}(t_m). \quad (13)$$

544 The hexasymmetry H could be generated by various properties of the cells, but H as defined above
545 contains also contributions from the hexasymmetry of the underlying trajectory. This is due to the fact
546 that we sum up in Eq. (10) the population activities $\bar{A}(t_m)$ without taking into account the distribution
547 of movement directions θ_m . In this way, a hexasymmetry that is potentially contained in the subject's
548 navigation trajectory contributes to the hexasymmetry H of the neural activity.

549 Empirical (fMRI/iEEG) studies (e.g. Doeller et al., 2010; Kunz et al., 2015) addressed this problem of
550 trajectories spuriously contributing to hexasymmetry by binning the movement direction and normalizing
551 the summed neural activity by the total time the subject moved in the respective movement-direction
552 bin. However, this procedure has the disadvantage that the derived hexasymmetry depends on the
553 parameters of binning, e.g. the angular resolution and the placement of bins. Moreover, the estimated
554 hexasymmetry is biased by uneven coverage of bins — with a failure of the procedure if a bin has
555 no entry, which prohibits a generalization to arbitrary narrow bins. In contrast, our new approach to
556 hexasymmetry in Eq. (12) has the advantage that it is independent of any discretization of movement
557 direction and that it allows an analytical treatment (see next section).

558 To nevertheless be able to quantify how much a specific trajectory contributed to the neural hex-
559 asymmetry $H = \left| \tilde{A}_6 \right|$, we also explicitly quantified the hexasymmetry of navigation trajectories and
560 interpreted H relative to the path hexasymmetry. To quantify the hexasymmetry of a trajectory, we
561 used the same approach as in Eq. (10) and defined the distribution of movement directions of the tra-
562 jectory by

$$\tilde{T}(\phi) = \frac{1}{M} \sum_{m=0}^{M-1} \delta(\phi - \theta_m). \quad (14)$$

563 The hexasymmetry of the trajectory is then $\left| \tilde{T}_6 \right| := \left| \frac{1}{M} \sum_{m=0}^{M-1} \exp(-6j\theta_m) \right|$, which is similar to Eq. (12).
564 To be able to estimate how much of the hexasymmetry H of neuronal activity is due to the hexasymmetry
565 of the trajectory, we compare the relative hexasymmetry of the activity, $\left| \tilde{A}_6 / \tilde{A}_0 \right|$, with the relative
566 hexasymmetry of the trajectory, $\left| \tilde{T}_6 / \tilde{T}_0 \right|$, noting that $\tilde{T}_0 \equiv 1$. The two terms being similar in magnitude,
567 i.e. $\left| \tilde{A}_6 / \tilde{A}_0 \right| \approx \left| \tilde{T}_6 \right|$, indicates that the trajectory is a major source of hexasymmetry whereas $H =$
568 $\left| \tilde{A}_6 \right| \gg \tilde{A}_0 \left| \tilde{T}_6 \right|$ suggests that hexasymmetry has a neural origin.

569 5.4.1 Analytical derivation of mean activity

570 In the following, we provide derivations that allow us to analytically integrate Eq. (9) for the conjunc-
571 tive grid by head-direction cell hypothesis and the structure-function mapping hypothesis but not for
572 the repetition suppression hypothesis. The respective results are shown in Fig. 2B–H and Fig. 4A–C,
573 demonstrating that they are very similar to the numerical results.

574 We analytically calculate the mean activity \bar{A} by averaging A along a linear segment of a trajectory
 575 (cf. Eq. (9)). For convenience, the following abbreviations are used in Eq. (2) with the same grid spacing,
 576 $s_i = s$, and the same grid orientation, $\gamma_i = \gamma$, for all cells i :

$$a := \frac{4\pi}{\sqrt{3}s} \quad (15)$$

$$b_{x,i} := s x_{\text{off},i}, \quad b_{y,i} := s y_{\text{off},i} \quad (16)$$

$$c_{k,x} := \sin\left(\frac{\pi}{3}k + \gamma\right), \quad c_{k,y} := \cos\left(\frac{\pi}{3}k + \gamma\right). \quad (17)$$

577 A single grid cell

578 We start with a single grid cell without head-direction tuning and without repetition suppression. Eq. (2)
 579 can be described in polar coordinates

$$G_i(r_t, \psi_t) = \frac{A_{\max}}{8} \prod_{k=0}^2 (1 + \cos[a c_{k,x} (r_t \cos(\psi_t) - b_{x,i}) + a c_{k,y} (r_t \sin(\psi_t) - b_{y,i})]). \quad (18)$$

580 In order to integrate along a piece of a straight line through the origin (similarly to the star-like walk),
 581 the angle $\psi_t \equiv \bar{\psi}$ can now be kept fixed (for that particular straight line) and we only have to consider
 582 $G_i(r_t, \bar{\psi})$. If we define r_m and r_{m+1} as the distances from zero that the subject is located at at times t_m
 583 and t_{m+1} respectively, integration by substitution gives us

$$\int_{t_m}^{t_{m+1}} dt r'_t G_i(r_t, \bar{\psi}) = \int_{r_m}^{r_{m+1}} dr G_i(r, \bar{\psi}). \quad (19)$$

584 Since the speed of movement $r'_t \equiv v$ is assumed to be constant along the whole trajectory and $\Delta r = v\Delta t$,
 585 for $\Delta r := r_{m+1} - r_m$, we obtain

$$\frac{1}{\Delta t} \int_{t_m}^{t_{m+1}} dt G_i(r_t, \bar{\psi}) = \frac{1}{\Delta t} \cdot \frac{1}{v} \int_{r_m}^{r_{m+1}} dr G_i(r, \bar{\psi}) = \frac{1}{\Delta r} \int_{r_m}^{r_{m+1}} dr G_i(r, \bar{\psi}). \quad (20)$$

586

587

588 Thus, we have

$$\bar{A}(t_m) = \frac{1}{\Delta r} \int_{r_m}^{r_{m+1}} dr G_i(r, \bar{\psi}) = \quad (21)$$

$$= \frac{1}{\Delta r} \frac{A_{\max}}{8} \int_{r_m}^{r_{m+1}} dr \prod_{k=0}^2 (1 + \cos[a c_{k,x} (r \cos(\bar{\psi}) - b_{x,i}) + a c_{k,y} (r \sin(\bar{\psi}) - b_{y,i})]) = \quad (22)$$

$$= \frac{1}{\Delta r} \frac{A_{\max}}{8} \left(\underbrace{\int_{r_m}^{r_{m+1}} dr 1}_{=:(A)} + \sum_{k=0}^2 \underbrace{\int_{r_m}^{r_{m+1}} dr z_k(r)}_{=:(B_k)} + \underbrace{\int_{r_m}^{r_{m+1}} dr z_0(r) z_1(r)}_{=:(C_{0,1})} \right) \quad (23)$$

$$+ \underbrace{\int_{r_m}^{r_{m+1}} dr z_0(r) z_2(r)}_{=:(C_{0,2})} + \underbrace{\int_{r_m}^{r_{m+1}} dr z_1(r) z_2(r)}_{=:(C_{1,2})} + \underbrace{\int_{r_m}^{r_{m+1}} dr z_0(r) z_1(r) z_2(r)}_{=:(D)}, \quad (24)$$

589 where $z_k(r) := \cos[a c_{k,x} (r \cos(\bar{\psi}) - b_{x,i}) + a c_{k,y} (r \sin(\bar{\psi}) - b_{y,i})]$. The four parts (A) – (D) are inte-

590 grated separately. We obtain

$$(A) = r \Big|_{r_m}^{r_{m+1}} \quad (25)$$

$$(B_k) = \begin{cases} \sin(r d_k - e_k) \cdot \frac{1}{d_k} \Big|_{r_m}^{r_{m+1}} & \text{if } d_k \neq 0 \\ \cos(e_k) r \Big|_{r_m}^{r_{m+1}} & \text{if } d_k = 0 \end{cases} \quad (26)$$

$$(C_{k,l}) = \begin{cases} \frac{1}{2} \left[\sin(r(d_k + d_l) - (e_k + e_l)) \frac{1}{d_k + d_l} + \sin(r(d_k - d_l) - (e_k - e_l)) \frac{1}{d_k - d_l} \right] \Big|_{r_m}^{r_{m+1}} & \text{if } d_k \neq \pm d_l \\ \left[\sin(2r d_k - e_k - e_l) + 2r d_k \cos(e_k - e_l) \right] \cdot \frac{1}{4d_k} \Big|_{r_m}^{r_{m+1}} & \text{if } d_k = d_l \neq 0 \\ \left[\sin(2r d_k - e_k + e_l) + 2r d_k \cos(e_k + e_l) \right] \cdot \frac{1}{4d_k} \Big|_{r_m}^{r_{m+1}} & \text{if } d_k = -d_l \neq 0 \\ r \cos(e_k) \cos(e_l) \Big|_{r_m}^{r_{m+1}} & \text{if } d_k = d_l = 0 \end{cases} \quad (27)$$

$$(D) = \begin{cases} \frac{1}{4} \left[\sin[(d_0 + d_1 + d_2)r - (e_0 + e_1 + e_2)] \frac{1}{d_0 + d_1 + d_2} \right. \\ \quad + \sin[(d_0 + d_1 - d_2)r - (e_0 + e_1 - e_2)] \frac{1}{d_0 + d_1 - d_2} \\ \quad + \sin[(d_0 - d_1 + d_2)r - (e_0 - e_2 + e_2)] \frac{1}{d_0 - d_1 + d_2} \\ \quad \left. + \sin[(d_0 - d_1 - d_2)r - (e_0 - e_1 - e_2)] \frac{1}{d_0 - d_1 - d_2} \right] \Big|_{r_m}^{r_{m+1}} & \text{if none of the denominators is zero} \\ \text{same as above with any term of the form} \\ \quad \sin[(d_0 \pm d_1 \pm d_2)r - (e_0 \pm e_1 \pm e_2)] \frac{1}{d_0 \pm d_1 \pm d_2} \\ \quad \text{replaced by } \cos(e_0 \pm e_1 \pm e_2)r & \text{if } d_0 \pm d_1 \pm d_2 = 0 \end{cases} \quad (28)$$

591 with the abbreviations

$$d_k = a (c_{k,x} \cos(\bar{\psi}) + c_{k,y} \sin(\bar{\psi})) \quad (29)$$

$$e_k = a (c_{k,x} b_{x,i} + c_{k,y} b_{y,i}). \quad (30)$$

592 Note that e_k actually depends on the cell index i which is omitted in Eqs. (25) - (28) in order to keep
593 the notation simpler.

594

595 **Head-direction tuning**

596 For a conjunctive grid by head-direction cell, the head-direction tuning depends only on the angle (which
597 is fixed when integrating along a straight line through zero) and not at all on the distance from zero.
598 The mean activity is thus obtained from the mean activity of a grid cell without head-direction tuning
599 by multiplying it with $h(\theta)$ defined in Eq. (4):

$$\frac{1}{\Delta r} \int_{r_m}^{r_{m+1}} dr G_i(r, \bar{\psi}) h_i(\bar{\psi}) = \frac{1}{\Delta r} h_i(\bar{\psi}) \int_{r_m}^{r_{m+1}} dr G_i(r, \bar{\psi}). \quad (31)$$

600

601

602 **Many cells**

603 For more than one cell, the total mean activity (population rate) can simply be calculated as the sum of

604 the mean activities of the single cells

$$\frac{1}{\Delta r} \int_{r_m}^{r_{m+1}} dr \sum_{i=1}^N G_i(r, \bar{\psi}) h_i(\bar{\psi}) = \frac{1}{\Delta r} \sum_{i=1}^N h_i(\bar{\psi}) \int_{r_m}^{r_{m+1}} dr G_i(r, \bar{\psi}). \quad (32)$$

605

606

607 Trajectories

608 The derived analytical description of the mean activity can be applied only to pieces of linear trajectories
609 through zero. For the star-like walk, we can simply integrate

$$\frac{1}{r_{\max}} \int_0^{r_{\max}} dr G_i(r, \theta) \quad \text{for } \theta \in \left\{ 0, \frac{2\pi}{N_\theta}, 2\frac{2\pi}{N_\theta} \dots \right\}. \quad (33)$$

610 Piece-wise linear trajectories and random walk trajectories consist of segments of straight lines that do
611 not necessarily pass through zero. In order to integrate along the m -th segment of a trajectory from
612 (x_{t_m}, y_{t_m}) to $(x_{t_{m+1}}, y_{t_{m+1}})$ with movement direction θ_m , we shift this path segment to the origin by
613 subtracting (x_{t_m}, y_{t_m}) from the grid offset $(x_{\text{off}}, y_{\text{off}})$ and then integrating

$$\frac{1}{r_{m+1}} \int_0^{r_{m+1}} dr G_i(r, \theta_m), \quad (34)$$

614 where $r_{m+1} = \sqrt{(x_{t_{m+1}} - x_{t_m})^2 + (y_{t_{m+1}} - y_{t_m})^2}$.

615 5.4.2 Upper bound for hexasymmetry of path trajectories

616 In the following we derive approximations for the expected value of the hexasymmetry $|\tilde{T}_6|$ of a path
617 trajectory described by the number of time steps M , the movement tortuosity σ_θ , and the time step size
618 Δt . These approximations can be used to assess the contribution of the underlying trajectory to the
619 overall hexasymmetry of neural activity.

620 From the definition of the Fourier coefficients in Eq. (11) and the movement direction distribution in
621 Eq. (14), we get the sixth Fourier coefficient of a trajectory:

$$\begin{aligned} \tilde{T}_6 &= \int_0^{2\pi} d\phi \frac{1}{M} \sum_{m=0}^{M-1} \delta(\phi - \theta_m) \exp(-6j\phi) \\ &= \frac{1}{M} \sum_{m=0}^{M-1} \exp(-6j\theta_m) = \frac{1}{M} \left(\sum_{m=0}^{M-1} \cos(6\theta_m) - j \sum_{m=0}^{M-1} \sin(6\theta_m) \right). \end{aligned} \quad (35)$$

622 The hexasymmetry of the trajectory can thus be expressed as

$$|\tilde{T}_6| = \frac{1}{M} \sqrt{\left(\sum_{m=0}^{M-1} \cos(6\theta_m) \right)^2 + \left(\sum_{m=0}^{M-1} \sin(6\theta_m) \right)^2}. \quad (36)$$

623 We simplify the sum of squares in Eq. (36)

$$\begin{aligned}
 \left(\sum_{m=0}^{M-1} \cos(6\theta_m) \right)^2 + \left(\sum_{m=0}^{M-1} \sin(6\theta_m) \right)^2 &= \sum_{m=0}^{M-1} (\cos(6\theta_m))^2 + 2 \sum_{m_1=0}^{M-1} \sum_{m_2=m_1+1}^{M-1} \cos(6\theta_{m_1}) \cos(6\theta_{m_2}) \\
 &\quad + \sum_{m=0}^{M-1} (\sin(6\theta_m))^2 + 2 \sum_{m_1=0}^{M-1} \sum_{m_2=m_1+1}^{M-1} \sin(6\theta_{m_1}) \sin(6\theta_{m_2}) \\
 &= M + \sum_{m_1=0}^{M-1} \sum_{\substack{m_2=0 \\ m_2 \neq m_1}}^{M-1} \cos(6(\theta_{m_1} - \theta_{m_2})) \tag{37}
 \end{aligned}$$

624 with the help of the multinomial theorem and the trigonometric identity $\cos(\alpha - \beta) = \cos(\alpha)\cos(\beta) +$
 625 $\sin(\alpha)\sin(\beta)$. If $\mathbb{E}(\cos(6(\theta_{m_1} - \theta_{m_2})))$ is known, we can compute the expected value of the square of the
 626 hexasymmetry of the path trajectory as

$$\begin{aligned}
 \mathbb{E} \left(|\tilde{T}_6|^2 \right) &= \mathbb{E} \left(\frac{1}{M^2} \left(M + \sum_{m_1=0}^{M-1} \sum_{\substack{m_2=0 \\ m_2 \neq m_1}}^{M-1} \cos(6(\theta_{m_1} - \theta_{m_2})) \right) \right) \\
 &= \frac{1}{M^2} \left(M + \sum_{m_1=0}^{M-1} \sum_{\substack{m_2=0 \\ m_2 \neq m_1}}^{M-1} \mathbb{E}(\cos(6(\theta_{m_1} - \theta_{m_2}))) \right). \tag{38}
 \end{aligned}$$

627 As $\mathbb{E}(X^2) = (\mathbb{E}(X))^2 + \text{Var}(X)$ for any random variable X , we can use the result in (38) to obtain the
 628 upper bound

$$\mathbb{E} \left(|\tilde{T}_6| \right) \leq \sqrt{\mathbb{E} \left(|\tilde{T}_6|^2 \right)}. \tag{39}$$

629 In the following, we focus on the derivation of $\mathbb{E}(\cos(6(\theta_{m_1} - \theta_{m_2})))$. Using the movement statistics

$$\Delta W \sim \mathcal{N}(0, \Delta t) \tag{40}$$

$$\theta_{t+\Delta t} = \theta_t + \sigma_\theta \Delta W \tag{41}$$

630 that were introduced below Eq. (1), the distribution of θ_m (after m time steps) can be derived when we
 631 start at some angle θ_0 :

$$\begin{aligned}
 \theta_1 &= \theta_0 + \sigma_\theta \Delta W \sim \mathcal{WN}(\theta_0, \sigma_\theta^2 \Delta t), \\
 \theta_2 &= \theta_1 + \sigma_\theta \Delta W \sim \mathcal{WN}(\theta_0, 2\sigma_\theta^2 \Delta t) \\
 &\vdots \\
 \theta_m &\sim \mathcal{WN}(\theta_0, m\sigma_\theta^2 \Delta t) \tag{42}
 \end{aligned}$$

632 where $\mathcal{WN}(\mu, \sigma^2)$ denotes the wrapped normal distribution with parameters μ and σ^2 , which correspond
 633 to the mean and variance of the corresponding unwrapped distribution (Jammalamadaka and Sengupta,
 634 2001).

635 In the following, we will derive the probability distribution of $\theta_{m_1} - \theta_{m_2}$. We first define $X_{m_1} \sim$
 636 $\mathcal{N}(\theta_0, m_1\sigma_\theta^2 \Delta t)$ and $X_{m_2} \sim \mathcal{N}(\theta_0, m_2\sigma_\theta^2 \Delta t)$ as the unwrapped versions of θ_{m_1} and θ_{m_2} , respectively, and
 637 $G_{X_{m_1} - X_{m_2}}$ as the distribution function of their difference $X_{m_1} - X_{m_2}$. Then, the distribution function

638 (Fisher, 1995) of $\theta_{m_1} - \theta_{m_2}$ reads as

$$F_{\theta_{m_1} - \theta_{m_2}}(z) = \sum_{k=-\infty}^{\infty} [G_{X_{m_1} - X_{m_2}}(z + 2\pi k) - G_{X_{m_1} - X_{m_2}}(2\pi k)] \quad (43)$$

$$= \sum_{k=-\infty}^{\infty} \left[\iint_{x-y \leq z+2\pi k} f_{X_{m_1}, X_{m_2}}(x, y) dx dy - \iint_{x-y \leq 2\pi k} f_{X_{m_1}, X_{m_2}}(x, y) dx dy \right] \quad (44)$$

$$= \sum_{k=-\infty}^{\infty} \left[\int_{-\infty}^{\infty} \int_{-\infty}^{z+2\pi k+y} f_{X_{m_1}, X_{m_2}}(x, y) dx dy - \int_{-\infty}^{\infty} \int_{-\infty}^{2\pi k+y} f_{X_{m_1}, X_{m_2}}(x, y) dx dy \right] \quad (45)$$

$$= \sum_{k=-\infty}^{\infty} \int_{-\infty}^{\infty} \int_{2\pi k+y}^{z+2\pi k+y} f_{X_{m_1}, X_{m_2}}(x, y) dx dy \quad (46)$$

639 where $f_{X_{m_1}, X_{m_2}}(x, y)$ is the joint probability distribution.

640 In order to calculate the distribution of $\theta_{m_1} - \theta_{m_2}$, we have to take the dependence between the two
 641 angles θ_{m_1} and θ_{m_2} into account. We will first consider the case $m_1 > m_2$. In this case, the conditional
 642 distribution of θ_{m_1} given $\theta_{m_2} = y$ is wrapped normal with conditional mean $\mathbb{E}(\theta_{m_1} | \theta_{m_2} = y) = y$ and
 643 conditional variance $\text{Var}(\theta_{m_1} | \theta_{m_2} = y) = (m_1 - m_2)\sigma_{\theta}^2 \Delta t$. The same can be said about the unwrapped
 644 versions of θ_{m_1} and θ_{m_2} . We will use this result to calculate the joint probability distribution

$$f_{X_{m_1}, X_{m_2}}(x, y) = f_{X_{m_1}}(x | X_{m_2} = y) f_{X_{m_2}}(y). \quad (47)$$

645 By applying the Leibniz integral rule in (*) we obtain the probability density of $\theta_{m_1} - \theta_{m_2}$:

$$f_{\theta_{m_1} - \theta_{m_2}}(z) = \frac{d}{dz} F_{\theta_{m_1} - \theta_{m_2}}(z) = \frac{d}{dz} \sum_{k=-\infty}^{\infty} \int_{-\infty}^{\infty} \int_{2\pi k+y}^{z+2\pi k+y} f_{X_{m_1}, X_{m_2}}(x, y) dx dy \quad (48)$$

$$\stackrel{(*)}{=} \sum_{k=-\infty}^{\infty} \int_{-\infty}^{\infty} f_{X_{m_1}, X_{m_2}}(z + 2\pi k + y, y) dy \quad (49)$$

$$= \sum_{k=-\infty}^{\infty} \int_{-\infty}^{\infty} f_{X_{m_1}}(z + 2\pi k + y | X_{m_2} = y) f_{X_{m_2}}(y) dy \quad (50)$$

$$= \sum_{k=-\infty}^{\infty} \int_{-\infty}^{\infty} \frac{1}{\sigma_{\theta} \sqrt{2\pi(m_1 - m_2)\Delta t}} \exp\left(-\frac{(z + 2\pi k + y - y)^2}{2(m_1 - m_2)\sigma_{\theta}^2 \Delta t}\right) \quad (51)$$

$$\cdot \frac{1}{\sigma_{\theta} \sqrt{2\pi m_2 \Delta t}} \exp\left(-\frac{(y - \theta_0)^2}{2m_2 \sigma_{\theta}^2 \Delta t}\right) dy \quad (52)$$

$$= \sum_{k=-\infty}^{\infty} \left[\frac{1}{\sigma_{\theta} \sqrt{2\pi(m_1 - m_2)\Delta t}} \exp\left(-\frac{(z + 2\pi k)^2}{2(m_1 - m_2)\sigma_{\theta}^2 \Delta t}\right) \right] \cdot \underbrace{\int_{-\infty}^{\infty} f_{X_{m_2}}(y) dy}_{=1} \quad (53)$$

646 For $m_2 > m_1$, we derive in the same way as above

$$f_{\theta_{m_1} - \theta_{m_2}}(z) = \sum_{k=-\infty}^{\infty} \int_{-\infty}^{\infty} f_{X_{m_1}}(z + 2\pi k + y) f_{X_{m_2}}(y | X_{m_1} = z + 2\pi k + y) dy$$

$$= \sum_{k=-\infty}^{\infty} \frac{1}{\sigma_{\theta} \sqrt{2\pi(m_2 - m_1)\Delta t}} \exp\left(-\frac{(z + 2\pi k)^2}{2(m_2 - m_1)\sigma_{\theta}^2 \Delta t}\right). \quad (54)$$

647 Finally, for $m_2 = m_1$, we have $\theta_{m_2} = \theta_{m_1}$. Altogether, we thus get

$$\theta_{m_1} - \theta_{m_2} \sim \mathcal{WN}(0, |m_1 - m_2| \sigma_\theta^2 \Delta t). \quad (55)$$

648 In order to calculate an upper bound for the average path hexasymmetry, we will now use Eq. (55)
649 in Eq. (38). Since $\mathbb{E}(\Re(Z)) = \Re(\mathbb{E}(Z))$ for a complex random variable Z and the n -th moment of a
650 wrapped normal distribution with parameters μ and σ^2 is $\mathbb{E}(\exp(j X)^n) = \exp(j n \mu - \frac{1}{2} n^2 \sigma^2)$, we can
651 derive

$$\begin{aligned} \mathbb{E}(\cos(6(\theta_{m_1} - \theta_{m_2}))) &= \mathbb{E}(\Re(\exp(j 6 (\theta_{m_1} - \theta_{m_2})))) = \Re(\mathbb{E}(\exp(j (\theta_{m_1} - \theta_{m_2}))^6)) \\ &= \Re\left(\exp\left(j 6 \mu_{m_1, m_2} - \frac{1}{2} 36 \sigma_{m_1, m_2}^2\right)\right) = \exp\left(-\frac{1}{2} 36 \sigma_{m_1, m_2}^2\right), \end{aligned} \quad (56)$$

652 where $\mu_{m_1, m_2} := 0$ and $\sigma_{m_1, m_2}^2 := |m_1 - m_2| \sigma_\theta^2 \Delta t$. We thus obtain

$$\begin{aligned} \mathbb{E}\left(|\tilde{T}_6|^2\right) &= \frac{1}{M^2} \left(M + \sum_{m_1=0}^{M-1} \sum_{\substack{m_2=0 \\ m_2 \neq m_1}}^{M-1} \exp\left(-\frac{1}{2} 36 \sigma_{m_1, m_2}^2\right) \right) \\ &= \frac{1}{M^2} \left(M + \sum_{m_1=0}^{M-1} \sum_{\substack{m_2=0 \\ m_2 \neq m_1}}^{M-1} \exp\left(-\frac{1}{2} 36 |m_1 - m_2| \sigma_\theta^2 \Delta t\right) \right). \end{aligned} \quad (57)$$

653 The solid lines in Figure S1 show the square root of Eq. (57) (cf. Eq. (39)).

654 From Eq. (57) we can derive simplified approximations for two limiting cases. For convenience, we use
655 $\alpha := \frac{1}{2} 36 \sigma_\theta^2 \Delta t$. First, if $\alpha \gg 1$, i.e. if the new direction after one step is almost uniformly distributed
656 or independent of the previous direction, we can neglect the double sum and we have

$$\mathbb{E}\left(|\tilde{T}_6|\right) \leq \frac{1}{\sqrt{M}}. \quad (58)$$

657 The corresponding line is shown in red in Figure S1. Note that in Figure S1 (with simulation step
658 size $\Delta t = 0.01$ s), $\alpha \gg 1$ corresponds to $\sigma_\theta \gg 2.36$. A comparison with results from numerical sim-
659 ulations shows that for any $\sigma_\theta > 3.5$ the Eq. (58) constitutes a viable upper bound of the mean path
660 hexasymmetry.

661 Second, we assume $M\alpha \gg 1$, i.e. the direction after M steps is almost independent from the original
662 direction. The double sum in Eq. (57) can then be approximated:

$$\sum_{m_1=0}^{M-1} \sum_{\substack{m_2=0 \\ m_2 \neq m_1}}^{M-1} \exp(-\alpha |m_1 - m_2|) = 2 \sum_{m_1=0}^{M-1} \sum_{m_2=m_1+1}^{M-1} \exp(-\alpha |m_1 - m_2|) \quad (59)$$

$$= 2 \sum_{m=1}^{M-1} (M - m) \exp(-\alpha m) \approx 2 \sum_{m=1}^{\infty} (M - m) \exp(-\alpha m) \quad (60)$$

$$= 2 \left(M \left(\sum_{m=0}^{\infty} (\exp(-\alpha))^m - 1 \right) - \sum_{m=1}^{\infty} m (\exp(-\alpha))^m \right) \quad (61)$$

$$= 2 \left(\frac{M}{\exp(\alpha) - 1} - \frac{\exp(\alpha)}{(\exp(\alpha) - 1)^2} \right), \quad (62)$$

663 where the first series in (61) is a geometric series and the second series is the polylogarithm function of

664 order -1. We further approximate

$$2 \left(\frac{M}{\exp(\alpha) - 1} - \frac{\exp(\alpha)}{(\exp(\alpha) - 1)^2} \right) \approx \frac{2M}{\exp(\alpha) - 1}. \quad (63)$$

665 For $\alpha \ll 1$, the error in the last approximation is $\frac{\exp(\alpha)}{(\exp(\alpha) - 1)^2} \approx \frac{1 + \alpha}{\alpha^2}$, which, if $M\alpha \gg 1$, is negligible
 666 compared to the remaining term $\frac{M}{\exp(\alpha) - 1}$. Since $\frac{\exp(\alpha)}{\exp(\alpha) - 1}$ is a strictly monotonically decreasing function
 667 of α , this approximation does not only hold for $\alpha \ll 1$ but is good in general.

668 Inserting Eq. (63) into Eq. (57) gives

$$\mathbb{E} \left(|\tilde{T}_6|^2 \right) = \frac{1}{M^2} \left(M + \frac{2M}{\exp(\alpha) - 1} \right) = \frac{1}{M} \left(1 + \frac{2}{\exp(\alpha) - 1} \right). \quad (64)$$

669 Hence, we get the approximation (for $M\alpha \gg 1$)

$$\mathbb{E} \left(|\tilde{T}_6| \right) \lesssim \sqrt{\frac{1}{M} \left(1 + \frac{2}{\exp(\alpha) - 1} \right)}. \quad (65)$$

670 This expression is used to compute the dashed lines in Figure S1, which all have slope $1/\sqrt{M}$ but a
 671 prefactor that depends on $\alpha = 18\sigma_\theta^2\Delta t$.

672 For $\alpha \ll 1$ (but still $M\alpha \gg 1$), we can use in Eq. (64) the first-order Taylor expansion of the
 673 exponential function at 0 to obtain

$$\frac{1}{M} \left(1 + \frac{2}{\exp(\alpha) - 1} \right) \approx \frac{1}{M} \left(1 + \frac{2}{\alpha} \right) \approx \frac{1}{M} \cdot \frac{2}{\alpha} = \frac{1}{M} \cdot \frac{1}{9\sigma_\theta^2\Delta t}. \quad (66)$$

674 Hence the path hexasymmetry for $\alpha \ll 1$ and $M\alpha \gg 1$ can be approximated by

$$\mathbb{E} \left(|\tilde{T}_6| \right) \lesssim \frac{1}{\sqrt{M}} \cdot \frac{1}{3\sigma_\theta\sqrt{\Delta t}}, \quad (67)$$

675 which allows us to see how the key variables M , σ_θ , and Δt interact in this limiting case. For instance,
 676 given a certain trajectory A with M_A steps and random walk parameters $\sigma_{\theta A}$ and Δt_A , we can use
 677 Eq. (67) to derive how many steps M_B are necessary in a second trajectory B with parameters $\sigma_{\theta B}$
 678 and Δt_B to achieve the same mean path hexasymmetry. From Eq. (67), we know that the two path
 679 hexasymmetries will have the same upper bound if

$$\frac{1}{\sqrt{M_A}} \cdot \frac{1}{3\sigma_{\theta A}\sqrt{\Delta t_A}} = \frac{1}{\sqrt{M_B}} \cdot \frac{1}{3\sigma_{\theta B}\sqrt{\Delta t_B}} \Leftrightarrow \frac{M_B}{M_A} = \frac{\sigma_{\theta A}^2\Delta t_A}{\sigma_{\theta B}^2\Delta t_B}. \quad (68)$$

680 Hence, the number of time steps M_A has to be multiplied by a factor $\Delta M := \frac{\sigma_{\theta A}^2\Delta t_A}{\sigma_{\theta B}^2\Delta t_B}$:

$$M_B = \Delta M \cdot M_A. \quad (69)$$

681 We illustrate the above considerations with an example: Let $\sigma_{\theta A} = 1 \text{ rad/s}^{1/2}$, $\sigma_{\theta B} = 0.5 \text{ rad/s}^{1/2}$
 682 and $\Delta t_A = \Delta t_B = 0.01 \text{ s}$. From the given values, we obtain

$$\Delta M = \frac{\sigma_{\theta A}^2\Delta t_A}{\sigma_{\theta B}^2\Delta t_B} = \frac{1}{0.25} = 4. \quad (70)$$

683 Thus, the mean hexasymmetry value of a trajectory with $\sigma_{\theta A} = 1$ after M_A time steps is the same as
 684 the mean hexasymmetry value of a trajectory with $\sigma_{\theta B} = 0.5$ after $M_B = 4 \cdot M_A$ time steps. Results

685 from numerical simulations of path hexasymmetries, shown in Figure S1, support the derived theoretical
686 approximations.

687 5.5 Random-field simulations

688 To quantitatively evaluate the structure-function mapping hypothesis, we set out to simulate a set of
689 grid cells in three-dimensional anatomical space. The grid phases associated with these grid cells follow
690 the correlation structure suggested by (Gu et al., 2018) and (Heys et al., 2014). Our aim is to quantify
691 the clustering of grid phases for a realistically-sized fMRI voxel given this correlation structure.

692 We use a three-dimensional representation of a voxel with a volume of $(3 \text{ mm})^3$. Within this voxel,
693 we define a grating of 200^3 potential grid cells that are equally spaced in the voxel, with a distance
694 between neighbouring cells of $15 \mu\text{m}$ along the axes of the grating. To generate a set of random but
695 spatially correlated grid phases on this area, we first define two random unit vectors in the complex
696 plane, \mathbf{Z}_1 and \mathbf{Z}_2 , for each of the 200^3 potential grid cells in the voxel; angles of the unit vectors are thus
697 drawn from a uniform distribution on the interval $[0, 2\pi)$. \mathbf{Z}_1 and \mathbf{Z}_2 are further resolved into their real
698 and imaginary components $\text{Re}(\mathbf{Z}_i)$ and $\text{Im}(\mathbf{Z}_i)$, respectively, where $i \in \{1, 2\}$. To generate correlations
699 between grid phases, we then convolve the two resulting gratings of 200^3 components separately with
700 either a Gaussian kernel (Fig. 4K) or a grid kernel (Fig. 4O) to yield the convolved components $\text{Re}(\hat{\mathbf{Z}}_i)$
701 and $\text{Im}(\hat{\mathbf{Z}}_i)$. The grid phases can be obtained by first calculating the angles of the new set of complex
702 numbers and normalizing the result by 2π :

$$\begin{aligned}\hat{x}_{\text{off}} &= \frac{\arg(\hat{\mathbf{Z}}_1)}{2\pi} \\ \hat{y}_{\text{off}} &= \frac{\arg(\hat{\mathbf{Z}}_2)}{2\pi}.\end{aligned}\tag{71}$$

703 We note that \hat{x}_{off} and \hat{y}_{off} are defined on the interval $[0, 1)$ and correspond to the grid phases of a single
704 grid cell mapped to the unit square. Transforming the result to the unit rhombus yields the grid phases
705 x_{off} and y_{off} in the x and y direction respectively:

$$\begin{aligned}x_{\text{off}} &= \hat{x}_{\text{off}} + \frac{\hat{y}_{\text{off}}}{2} \\ y_{\text{off}} &= \frac{\sqrt{3}}{2}\hat{y}_{\text{off}}\end{aligned}\tag{72}$$

706 To find the average pairwise grid phase distances as a function of the pairwise anatomical distances,
707 10^8 pairs of grid cells are sampled randomly from the uniform distribution defined on the discrete space
708 of grating cell positions. The Euclidean distance in anatomical space between the two grid cells in each
709 pair is calculated and sorted into 50 bins of equal width on the interval $[10, 500] \mu\text{m}$. Then, for each pair
710 of grid cells, n_1 and n_2 , 8 copies of the grid phase $(x_{\text{off},2}, y_{\text{off},2})$ of the second cell n_2 are made, which are
711 offset from the initial position of the grid phase such that they are positioned at the same phase within
712 unit rhombi laid end-to-end on a 3×3 grid. The minimum distance between the grid phase of the cell
713 n_1 and the grid phase of each of the copies of the cell n_2 is taken as the pairwise phase distance. Finally,
714 the pairwise distance between grid phase offsets per distance bin is obtained by taking the mean over all
715 grid cell pairs whose Euclidean distance in anatomical space falls into the corresponding bin (Fig. 4H,
716 L, P).

717 To estimate the clustering concentration parameter κ_s in Fig. 4, the phases \hat{x}_{off} and \hat{y}_{off} are mapped
718 to a circular distribution by multiplying them with 2π . The sets of grid phases $\{2\pi\hat{x}_{\text{off}}^i \mid i \in \{1, 2, \dots, N\}\}$
719 and $\{2\pi\hat{y}_{\text{off}}^i \mid i \in \{1, 2, \dots, N\}\}$ are then each separately fit to a one-dimensional von Mises distribution to
720 obtain a clustering concentration parameter for each axis. The final value of κ_s is taken as the average

721 of these two values.

Table 1: Parameters: descriptions and values.

Parameter	Description	Values (unless varied) or Range
Trajectories		
Δt	Simulation time step	0.01 s
T	Simulated duration	9000 s
v	Movement speed	10 cm/s
σ_θ	Movement tortuosity	0.5 rad/s ^{1/2}
r_{max}	Length of a linear path in the star-like run	300 cm
N_θ	Number of angles to sample in the star-like run	360
Grid cells		
N	Number of grid cells in a voxel	1024
s	Grid scale	30 cm
γ	Grid orientation	0°
A_{max}	Maximum firing rate for one grid cell	1 spk/s
(x_{off}, y_{off})	Grid phase (2-dimensional)	([0,1], [0,1])
Conjunctive grid by head-direction cell hypothesis		
μ_c	Preferred head direction	$[0, 2\pi)$ (multiples of 60° for $\sigma_c = 0$)
κ_c	Concentration parameter for direction tuning for the ideal and “realistic” ¹ cases	$\{50, 10\}$ rad ⁻²
σ_c	Alignment jitter of direction tuning to grid axis for the ideal and “realistic” ¹ cases	$\{0, 3\}^\circ$
p_c	Fraction of conjunctive cells in a population for the ideal and “realistic” ² cases	$\{1, 1/3\}$
Repetition suppression hypothesis		
τ_r	Adaptation time constant	$\{3, 1.5\}$ s
w_r	Adaptation weight for the ideal and “weaker” cases	$\{1, 0.5\}$
Structure-function mapping hypothesis		
μ_s	Central phase of cluster	(0, 0)
κ_s	Concentration parameter for clustering for the ideal and “realistic” ³ cases	$\{10, 0.1\}$

¹(Doeller et al., 2010)

²(Boccaro et al., 2010; Sargolini et al., 2006)

³(Gu et al., 2018)

722 Acknowledgements

723 We would like to thank Tiziano D’Albis for discussions.

724 This work was funded by the German Research Foundation (DFG, Project number 327654276 – SFB
725 1315 to RK), the German Federal Ministry of Education and Research (01GQ1705 to RK), and the
726 Einstein Foundation Berlin (to IK). LK received funding from the German Research Foundation (DFG;
727 KU 4060/1-1; Projektnummer 447634521), the Federal Ministry of Education and Research (BMBF;
728 01GQ1705A), and by NIH/NINDS grant U01 NS113198-01.

729 Author contributions

1. Conceptualisation	ER, RK, LK
2. Data Curation	IK, ER
3. Formal Analysis	IK, ER, NA
4. Funding Acquisition	RK, LK
5. Investigation	IK, ER, NA
6. Methodology	IK, ER, LK, NA, RK
7. Resources	RK, LK
8. Software	IK, ER, NA
9. Supervision	RK, LK, ER
10. Validation	IK, NA, ER
11. Visualisation	IK, ER, NA, LK
12. Writing - Original Draft Preparation	IK, ER, LK, RK, NA
13. Writing - Review & Editing	IK, ER, LK, RK, NA

References

- 730
- 731 A. Banino, C. Barry, B. Uria, C. Blundell, T. Lillicrap, P. Mirowski, A. Pritzel, M.J. Chadwick, T. De-
732 gris, J. Modayil, G. Wayne, H. Soyer, F. Viola, B. Zhang, R. Goroshin, N. Rabinowitz, R. Pascanu,
733 C. Beattie, S. Petersen, A. Sadik, S. Gaffney, H. King, K. Kavukcuoglu, D. Hassabis, R. Hadsell, and
734 D. Kumaran. Vector-based navigation using grid-like representations in artificial agents. *Nature*, 557:
735 429–433, 2018.
- 736 J.L.S Bellmund, L. Deuker, T.N. Schröder, and C.F. Doeller. Grid-cell representations in mental simu-
737 lation. *eLife*, 5:e17089, 2016.
- 738 A. Bierbrauer, L. Kunz, C.A. Gomes, M. Luhmann, L. Deuker, S. Getzmann, E. Wascher, P.D. Gajewski,
739 J.G. Hengstler, M. Fernandez-Alvarez, M. Atienza, D.M. Cammisuli, F. Bonatti, C. Pruneti, A. Perce-
740 sepe, Y. Bellaali, B. Hanseeuw, B.A. Strange, J.L. Cantero, and N. Axmacher. Unmasking selective
741 path integration deficits in Alzheimer’s disease risk carriers. *Science Advances*, 6:eaba1394, 2020.
- 742 C.N. Boccara, F. Sargolini, V.H. Thoresen, T. Solstad, M.P. Witter, E.I. Moser, and M.-B. Moser. Grid
743 cells in pre- and parasubiculum. *Nature Neuroscience*, 13:987–994, 2010.
- 744 A. Bongioanni, D. Folloni, L. Verhagen, J. Sallet, M.C. Klein-Flügge, and M.F.S. Rushworth. Activation
745 and disruption of a neural mechanism for novel choice in monkeys. *Nature*, 591:270–274, 2021.
- 746 D. Bush, C. Barry, D. Manson, and N. Burgess. Using grid cells for navigation. *Neuron*, 87:507–520,
747 2015.
- 748 D. Chen, L. Kunz, W. Wang, H. Zhang, W. Wang, A. Shulze-Bonhage, P.C. Reinacher, W. Zhou,
749 S. Liang, N. Axmacher, and L. Wang. Hexadirectional modulation of theta power in human entorhinal
750 cortex during spatial navigation. *Current Biology*, 28:3310–3315, 2018.
- 751 D. Chen, L. Kunz, P. Lv, H. Zhang, W. Zhou, S. Liang, N. Axmacher, and L. Wang. Theta oscillations
752 coordinate grid-like representations between ventromedial prefrontal and entorhinal cortex. *Science*
753 *Advances*, 7:eabj0200, 2021.
- 754 A.O. Constantinescu, J.X. O’Reilly, and T.E.J. Behrens. Organizing conceptual knowledge in humans
755 with a gridlike code. *Science*, 352:1464–1468, 2016.
- 756 T. D’Albis and R. Kempter. A single-cell spiking model for the origin of grid-cell patterns. *PLOS*
757 *Computational Biology*, 13:e1005782, 2017.
- 758 L. Deuker, J.L.S. Bellmund, T. Navarro Schröder, and C.F. Doeller. An event map of memory space in
759 the hippocampus. *eLife*, 5:e16534, 2016.
- 760 C.F. Doeller, C. Barry, and N. Burgess. Evidence for grid cells in a human memory network. *Nature*,
761 463:657–661, 2010.
- 762 A. Ekstrom. How and when the fMRI bold signal relates to underlying neural activity: The danger in
763 dissociation. *Brain Research Reviews*, 62:233–244, 2010.
- 764 N.I. Fisher. *Statistical analysis of circular data*. Cambridge University Press, 1995.
- 765 R. Gardner, E. Hermansen, M. Pachitariu, Y. Burak, N. Baas, B. Dunn, M.-B. Moser, and E.I. Moser.
766 Toroidal topology of population activity in grid cells. *Nature*, 602:123–128, 2022.
- 767 M. Gil, M. Ancau, M. I. Schlesiger, A. Neitz, K. Allen, R. J. De Marco, and H. Monyer. Impaired path
768 integration in mice with disrupted grid cell firing. *Nature Neuroscience*, 21:81–91, 2018.

- 769 K. Grill-Spector, R. Henson, and A. Martin. Repetition and the brain: neural models of stimulus-specific
770 effects. *Trends in Cognitive Sciences*, 10:14–23, 2006.
- 771 Y. Gu, S. Lewallen, A.A. Kinkhabwala, C. Domnisoru, K. Yoon, J.L. Gauthier, I.R. Fiete, and D.W.
772 Tank. A map-like micro-organization of grid cells in the medial entorhinal cortex. *Cell*, 175:736–750,
773 2018.
- 774 T. Hafting, M. Fyhn, S. Molden, M.-B. Moser, and E.I. Moser. Microstructure of a spatial map in the
775 entorhinal cortex. *Nature*, 436:801–806, 2005.
- 776 J.G. Heys, K.V. Rangarajan, and D.A. Dombeck. The functional micro-organization of grid cells revealed
777 by cellular-resolution imaging. *Neuron*, 84:1079–1090, 2014.
- 778 A.J. Horner, J.A. Bisby, E. Zotow, D. Bush, and N. Burgess. Grid-like processing of imagined navigation.
779 *Current Biology*, 26:842–847, 2016.
- 780 J. Jacobs, C.T. Weidemann, J.F. Miller, A. Solway, J.F. Burke, X.-X. Wei, N. Suthana, M.R. Sperling,
781 A.D. Sharan, I. Fried, and M.J. Kahana. Direct recordings of grid-like neuronal activity in human
782 spatial navigation. *Nature Neuroscience*, 16:1188–1190, 2013.
- 783 S.R. Jammalamadaka and A. Sengupta. *Topics in Circular Statistics*. World Scientific, 2001.
- 784 J.B. Julian and C.F. Doeller. Remapping and realignment in the human hippocampal formation predict
785 context-dependent spatial behavior. *Nature Neuroscience*, 24:863–872, 2021.
- 786 J.B. Julian, A.T. Keinath, G. Frazzetta, and R.A. Epstein. Human entorhinal cortex represents visual
787 space using a boundary-anchored grid. *Nature Neuroscience*, 21:191–194, 2018.
- 788 N.J. Killian, M.J. Jutras, and E.A. Buffalo. A map of visual space in the primate entorhinal cortex.
789 *Nature*, 491:761–764, 2012.
- 790 E. Kropff and A. Treves. The emergence of grid cells: Intelligent design or just adaptation? *Hippocampus*,
791 18:1256–1269, 2008.
- 792 L. Kunz, T.N. Schröder, H. Lee, C. Montag, B. Lachmann, R. Sariyska, M. Reuter, R. Stirnberg,
793 T. Stöcker, P.C. Messing-Floeter, J. Fell, C.F. Doeller, and N. Axmacher. Reduced grid-cell-like
794 representations in adults at genetic risk for Alzheimer’s disease. *Science*, 350:430–433, 2015.
- 795 L. Kunz, S. Maidenbaum, D. Chen, L. Wang, J. Jacobs, and N. Axmacher. Mesoscopic neural represen-
796 tations in spatial navigation. *Trends in Cognitive Sciences*, 23:615–630, 2019.
- 797 S. Maidenbaum, J. Miller, M. Stein Joel, and J. Jacobs. Grid-like hexadirectional modulation of human
798 entorhinal theta oscillations. *Proceedings of the National Academy of Sciences USA*, 115:10798–10803,
799 2018.
- 800 H. Moon, B. Gauthier, H. Park, N. Faivre, and O. Blanke. Sense of self impacts spatial navigation and
801 hexadirectional coding in human entorhinal cortex. *Communications Biology*, 5:1–12, 2022.
- 802 E.I. Moser, M.-B. Moser, and B.L. McNaughton. Spatial representation in the hippocampal formation:
803 a history. *Nature Neuroscience*, 20:1448–1464, 2017.
- 804 R. Mukamel, H. Gelbard, A. Arieli, U. Hasson, I. Fried, and R. Malach. Coupling between neuronal
805 firing, field potentials, and fMRI in human auditory cortex. *Science*, 309:951–954, 2005.

- 806 Z. Nadasdy, T.P. Nguyen, Á. Török, J.Y. Shen, D.E. Briggs, P.N. Modur, and R.J. Buchanan. Context-
807 dependent spatially periodic activity in the human entorhinal cortex. *Proceedings of the National*
808 *Academy of Sciences USA*, 114:E3516–E3525, 2017.
- 809 M. Nau, T. Navarro Schröder, J.L.S. Bellmund, and C.F. Doeller. Hexadirectional coding of visual space
810 in human entorhinal cortex. *Nature Neuroscience*, 21:188–190, 2018.
- 811 J. O’Keefe and J. Dostrovsky. The hippocampus as a spatial map: Preliminary evidence from unit
812 activity in the freely-moving rat. *Brain Research*, 34:171–175, 1971.
- 813 F. Sargolini, M. Fyhn, T. Hafting, B.L. McNaughton, M.P. Witter, M.-B. Moser, and E.I. Moser. Con-
814 junctive representation of position, direction, and velocity in entorhinal cortex. *Science*, 312:758–762,
815 2006.
- 816 B. Si, E. Kropff, and A. Treves. Grid alignment in entorhinal cortex. *Biological Cybernetics*, 106:483–506,
817 2012.
- 818 M. Stangl, J. Achtzehn, K. Huber, C. Dietrich, C. Tempelmann, and T Wolbers. Compromised grid-cell-
819 like representations in old age as a key mechanism to explain age-related navigational deficits. *Current*
820 *Biology*, 28:1108–1115, 2018.
- 821 T. Staudigl, M. Leszczynski, J. Jacobs, S.A. Sheth, C.E. Schroeder, O. Jensen, and C.F. Doeller. Hexadi-
822 rectional modulation of high-frequency electrophysiological activity in the human anterior medial tem-
823 poral lobe maps visual space. *Current Biology*, 28:3325–3329, 2018.
- 824 M. Stemmler, A. Mathis, and A.V.M. Herz. Connecting multiple spatial scales to decode the population
825 activity of grid cells. *Science Advances*, 1:e1500816, 2015.
- 826 H. Stensola, T. Stensola, T. Solstad, K. Frøland, M.-B. Moser, and E.I. Moser. The entorhinal grid map
827 is discretized. *Nature*, 492:72–78, 2012.
- 828 J.S. Taube, R.U. Muller, and J.B. Ranck. Head-direction cells recorded from the postsubiculum in freely
829 moving rats. II. Effects of environmental manipulations. *Journal of Neuroscience*, 10:436–474, 1990.
- 830 J.J. Tukker, P. Beed, M. Brecht, R. Kempster, E.I. Moser, and D. Schmitz. Microcircuits for spatial
831 coding in the medial entorhinal cortex. *Physiological Reviews*, 102:653–688, 2022.
- 832 L.K. Vass, M.S. Copara, M. Seyal, K. Shahlaie, S. Tomaszewski Farias, P.Y. Shen, and A.D. Ekstrom.
833 Oscillations go the distance: Low-frequency human hippocampal oscillations code spatial distance in
834 the absence of sensory cues during teleportation. *Neuron*, 89:1180–1186, 2016.
- 835 W. Wang and W. Wang. Effect of reward on electrophysiological signatures of grid cell population
836 activity in human spatial navigation. *Scientific Reports*, 11:1–9, 2021.

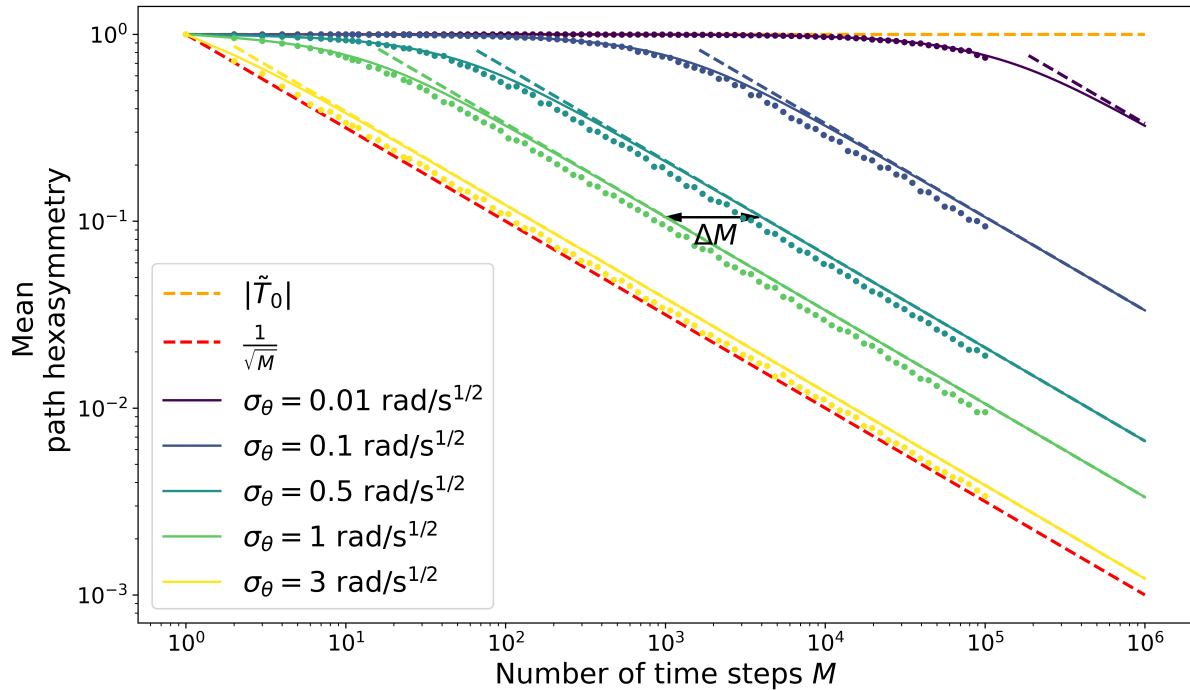


Figure S1: Hexasymmetry of random walk trajectories. The (horizontal) orange dashed line shows the offset (or maximum) of the path hexasymmetry, $\tilde{T}_0 \equiv 1$. The (diagonal) red dashed line shows the average path hexasymmetry $|\tilde{T}_6| = 1/\sqrt{M}$ associated with randomly sampling a movement direction at each time step from a uniform distribution on the interval $[0, 2\pi)$. Solid colored curves show an upper bound for the mean path hexasymmetry of a random walk as a function of the number of time steps (square root of Eq. (57)) for five different movement tortuosities σ_θ and a simulation time step size $\Delta t = 10$ ms. The corresponding five colored dashed lines show an approximation ($|\tilde{T}_6| \propto 1/\sqrt{M}$, Eq. (65)) to the solid curves; the approximation is excellent if the number M of time steps is large enough. Colored dots show the respective mean path hexasymmetries obtained from numerical simulations (Eq. (1)). The black arrow shows the multiplicative shift in the number of time steps that is necessary to obtain the same hexasymmetry for a trajectory with $\sigma_\theta = 0.5 \text{ rad/s}^{1/2}$ as for a trajectory with $\sigma_\theta = 1 \text{ rad/s}^{1/2}$, as derived in Eq. (70).

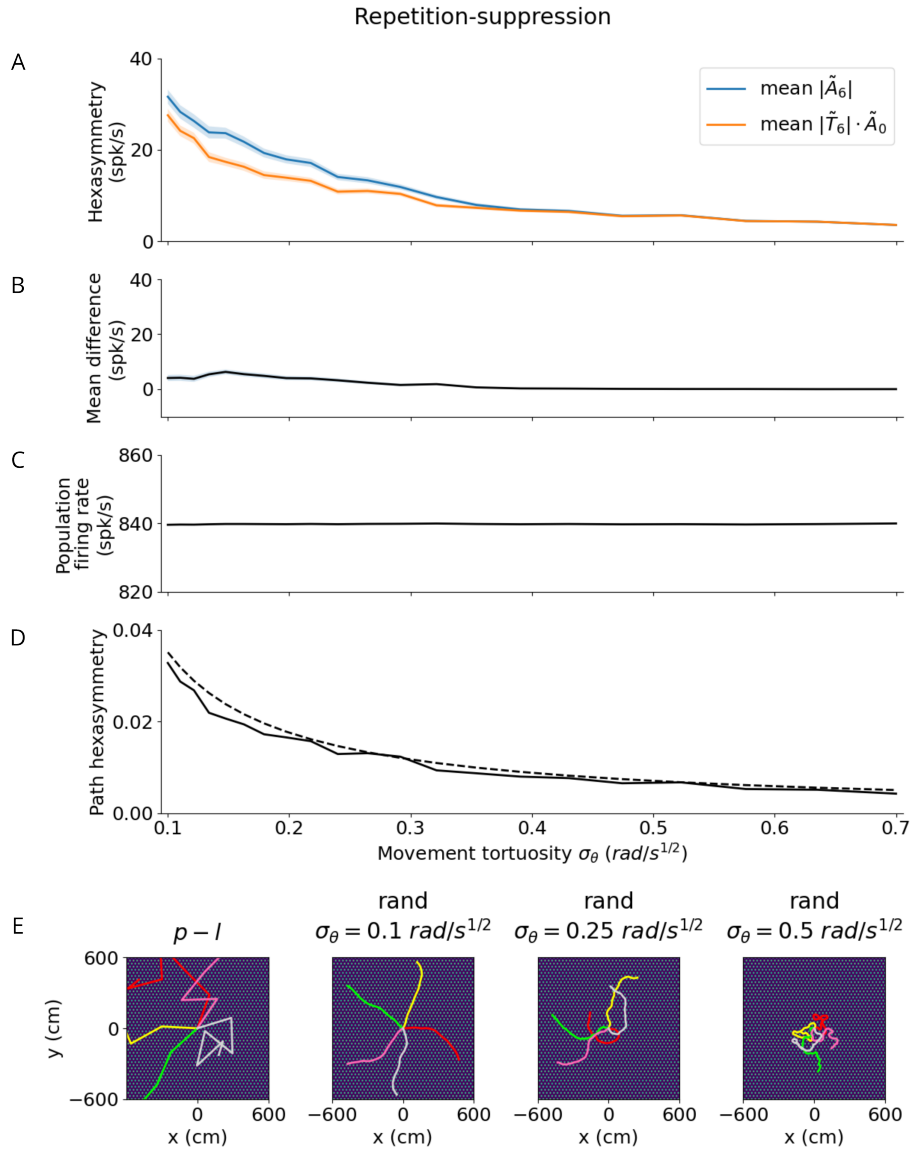


Figure S2: Effect of tortuosity on the hexasymmetry for the repetition-suppression hypothesis with random walks ($\Delta t = 0.01$ s, $T = 9000$ s, $\tau_r = 3$ s, $w_r = 1$). **(A)** The hexasymmetry $|\tilde{A}_6|$ (blue) and the scaled path hexasymmetry $|\tilde{T}_6| \cdot \tilde{A}_0$ (orange) as a function of the movement tortuosity σ_θ of a random walk. The shaded areas represent the standard error when averaging over 100 realizations of the trajectory, each with an initial direction sampled from a random uniform distribution on the interval $[0, 2\pi)$. **(B)** The mean difference between $|\tilde{A}_6|$ and $|\tilde{T}_6| \cdot \tilde{A}_0$ as a function of the movement tortuosity σ_θ . Note that $|\tilde{A}_6| \geq |\tilde{T}_6| \cdot \tilde{A}_0$ for $\sigma_\theta \leq 0.4$. For $\sigma_\theta > 0.4$ the two curves begin to overlap: repetition-suppression ceases to have a significant effect and the hexasymmetry $|\tilde{A}_6|$ is primarily dictated by the path hexasymmetry. The dip in the mean difference near $\sigma_\theta \sim 0.1$ is thought to be due to numerical noise. **(C)** The mean firing rate \tilde{A}_0 does not depend on movement tortuosity σ_θ , indicating that any effect of repetition-suppression on the population firing rate is small. **(D)** Path hexasymmetry $|\tilde{T}_6|$ as a function of the movement tortuosity σ_θ . The solid line depicts the mean path hexasymmetry averaged over 100 realizations of a trajectory, while the dashed line plots the analytical result in Eq. (65). **(E)** Leftmost panel: Five examples (colored line segments) of a piece-wise linear (“p-l”) trajectory; each linear path segment has a length of 300 cm. Three rightmost panels: Five example random walk (“rand”) trajectories (colored curves) for three different values of the movement tortuosity σ_θ with total simulation time $T = 60$ s and a total path length of 600 cm. For illustration purposes, the initial directions of example random walk trajectories were chosen such that they are regularly distributed on the interval $[0, 2\pi)$. When viewed on a scale within the range of ± 600 cm, increasing the tortuosity from 0.1 to 0.5 results in increasingly more curved trajectories. The bright dots in all panels of (E) show the grid fields with grid spacing 30 cm, which is small when viewed on this scale. In the simulations for Figs. 2–5, the random walk trajectories have total lengths of 90,000 cm or longer and use a movement tortuosity of $\sigma_\theta = 0.5 \text{ rad/s}^{1/2}$.

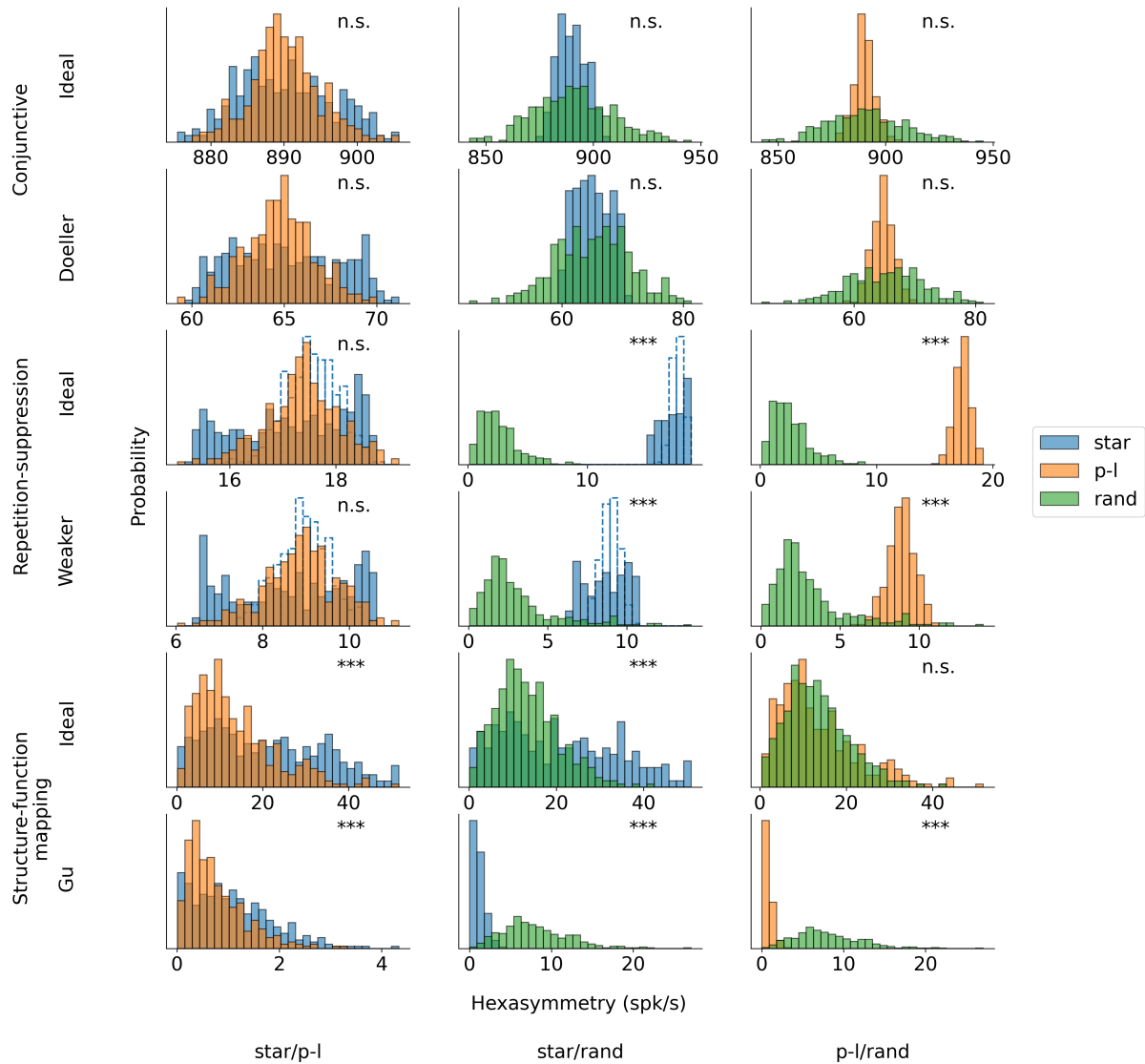


Figure S3: Pair-wise comparisons of the hexasymmetry values from different trajectory types for each set of parameters. The compared trajectory types are star-like walks (“star”), piecewise-linear walks (“p-l”), and random walks (“rand”). For each hypothesis, we calculate the hexasymmetry for ideal parameters (conjunctive: $p_c = 1$, $\kappa_c = 50 \text{ rad}^{-2}$, $\sigma_c = 0$; repetition suppression: $\tau_r = 3 \text{ s}$, $w_r = 1$; clustering: $\kappa_s = 10$) as well as more realistic parameters (conjunctive: $p_c = 0.33$, $\kappa_c = 10 \text{ rad}^{-2}$, $\sigma_c = 3^\circ$; repetition suppression: $\tau_r = 1.5 \text{ s}$, $w_r = 0.5$; clustering: $\kappa_s = 0.1$). In the case of the repetition-suppression hypothesis, the solid blue bars show the star-like walk with a carry-over of the repetition-suppression mechanism when teleporting between different path segments, while the transparent bars with the dotted blue borders represent the star-like walk with no carry-over of the repetition-suppression effect across different path segments. For the star-like walk, the starting phase of the star is sampled from a uniform distribution across the unit rhombus between realizations, and remains constant within each realization of the star-like walk trajectory. The direction of movement for both the star-like walk and the piece-wise linear walk is sampled randomly without replacement from the integer angles $\{0, 1, 2, \dots, 359\}^\circ$. The parameters for the random-walk scenario are $T = 9000 \text{ s}$ and $\Delta t = 0.01 \text{ s}$. Each hypothesis condition was simulated for 300 realizations. ***, $P < 0.001$; n.s., not significant. Note that the scales of the horizontal axes are different across subpanels.

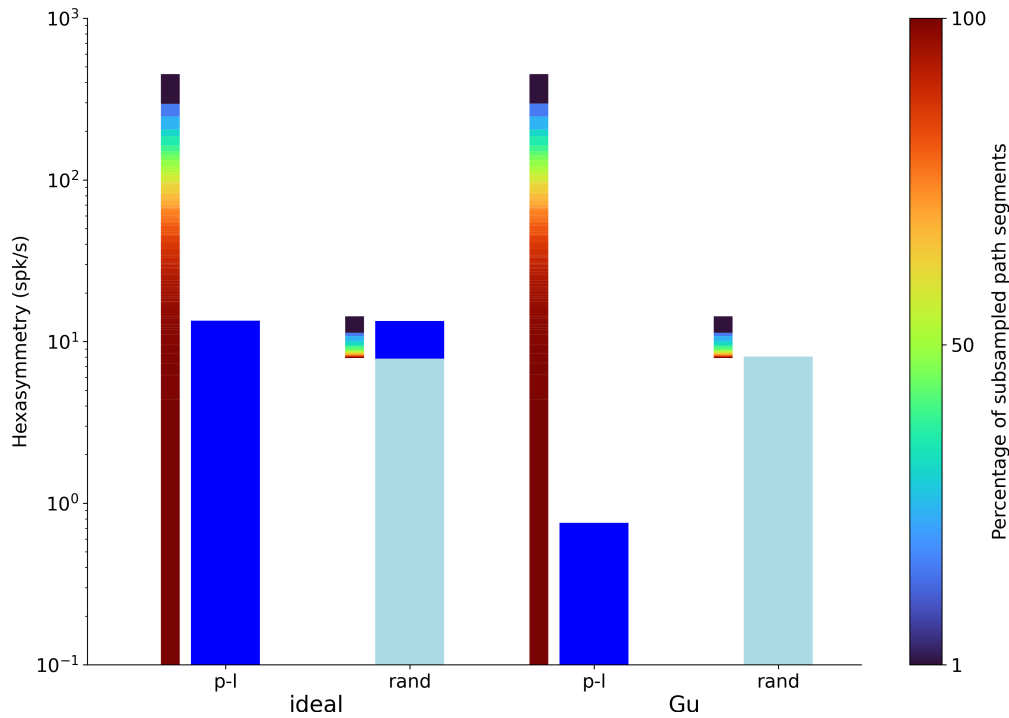


Figure S4: Hexasymmetry resulting from piece-wise linear walks (“p-l”) and random walks (“rand”) as a function of the percentage of subsampled path segments for the structure-function mapping hypothesis. Values of “ideal” parameters (left) and more realistic parameter values (“Gu”; right) are identical to the ones used in Fig. 5. The thinner gradient bars show the percentage of subsampled path segments required to produce the corresponding scaled path hexasymmetry $|\tilde{T}_6| \cdot \tilde{A}_0$. The thicker dark blue and light blue bars represent the hexasymmetry $|A_6|$ and the path hexasymmetry multiplied by the mean firing rate $|\tilde{T}_6| \cdot \tilde{A}_0$, respectively. The percentages of path segments were subsampled from 1% to 100% in steps of 1%. In the case of the random walk trajectories, e.g. subsampling 100% of the path segments yields $|\tilde{T}_6| \cdot \tilde{A}_0 = |A_6| = 7.92$ spk/s. For each percentage value, the path hexasymmetry was averaged over 100 different realizations of the piece-wise linear or random walk trajectory.

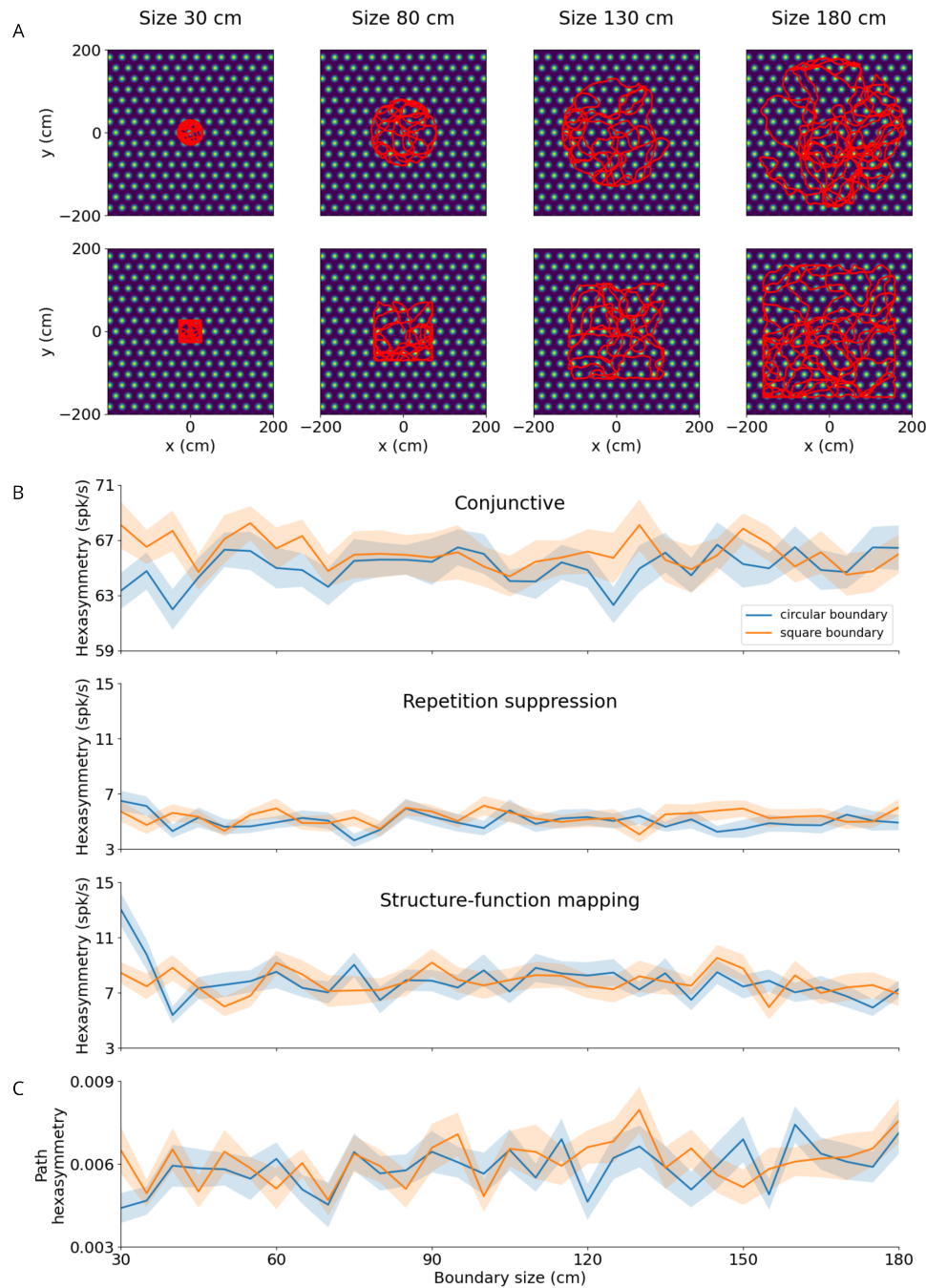


Figure S5: Effect of size and shape of finite environments on hexasymmetry. (A) Examples of bounded trajectories (red) within square boundaries (bottom; “size” indicates half of side length) or circular boundaries (top; “size” indicates radius) of varying sizes (increasing from left to right). Trajectories are overlaid on the firing field of an example grid cell. The lengths of the depicted trajectories are modified for illustration purposes, and do not reflect the full extent of trajectories used to calculate hexasymmetries. (B) Hexasymmetry for the three hypotheses for different sizes of the boundaries; blue, circular boundary; orange, square boundary. For the conjunctive grid by head-direction cell and structure-function mapping hypotheses, the “realistic” parameter sets were used, while the optimal parameter set was used for the repetition-suppression hypothesis; for values of the parameters, see Table 1. Overall, the obtained values of the hexasymmetry have a weak (if any) dependence on boundary shape and size (apart from fluctuations due to noise in different realizations), and the obtained values are similar in magnitude to those obtained in infinite environments: Fig. 2H for “conjunctive” (with a factor 3 difference due to 3-fold different values of p_c), Fig. 3E for “repetition suppression”, and Fig. 4C for “structure-function mapping”. (C) Path hexasymmetry for different sizes of the boundaries. In (B) and (C), lines represent the mean and shaded areas represent the standard error as obtained from 20 trajectories.

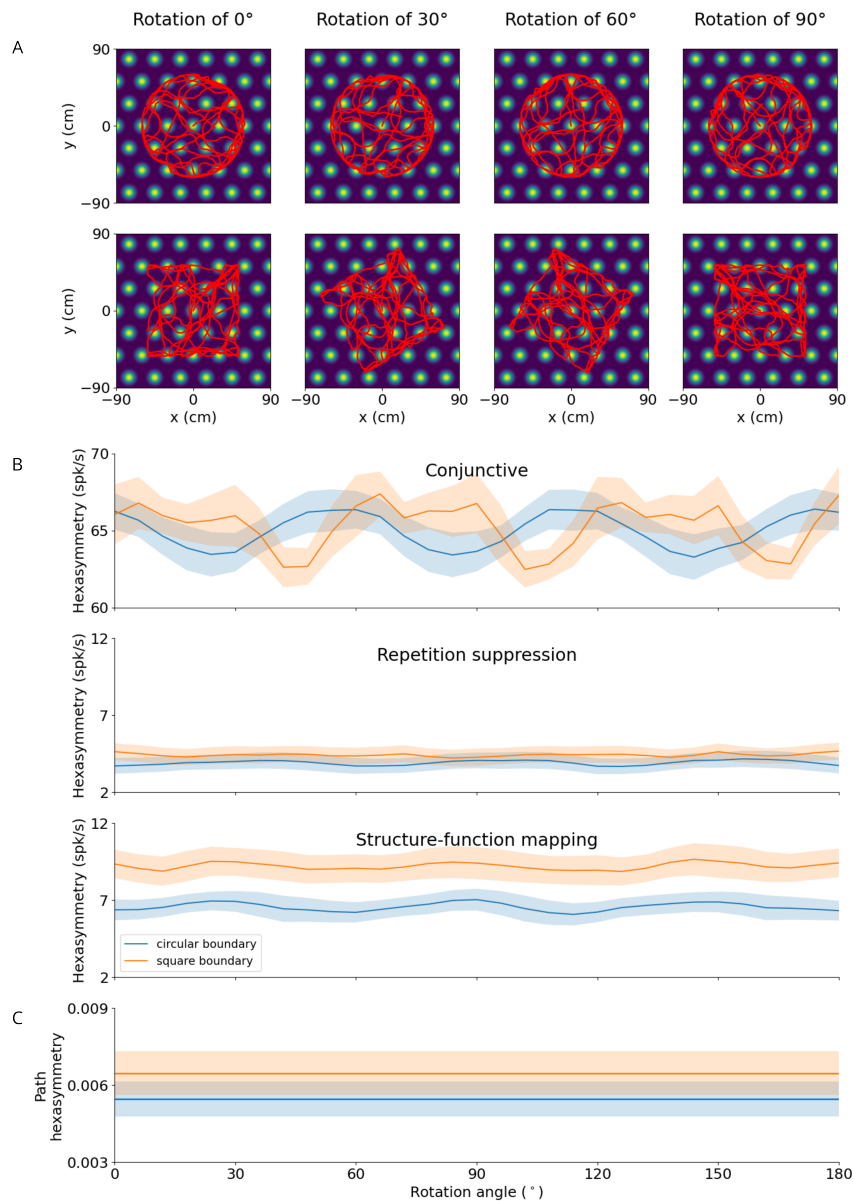


Figure S6: Effect of rotation of finite environments on hexasymmetry. (A) Examples of bounded trajectories (red) within circular (top) or square (bottom) boundaries for different rotation angles (numbers at top) relative to the grid orientation. Trajectories are overlaid on the firing field of an example grid cell. The lengths of the depicted trajectories are modified for illustration purposes, and do not reflect the full extent of trajectories used to calculate hexasymmetries. (B) Hexasymmetry for the three hypotheses for different rotation angles of the trajectory; blue: circular boundary; orange: square boundary. The periodic fluctuation in neural hexasymmetry for the conjunctive hypothesis with a square environment is due to the alignment of the edges of the square with the grid axes whenever the trajectory is rotated by multiples of 30° and 60° combined with the tendency of the subject to move along the walls of the boundary. With circular boundaries, these fluctuations are closer to the order of the standard error, and are due to a combination of directional bias in the trajectory and noise in the arrangement of grid phase offsets. Otherwise, the obtained values of the hexasymmetry have a weak (if any) dependence on boundary shape and orientation (apart from fluctuations due to noise in different realizations), and the obtained values are similar in magnitude to those obtained in infinite environments: Fig. 2H for “conjunctive” (with a factor 3 difference due to 3-fold different values of p_c), Fig. 3E for “repetition suppression”, and Fig. 4C for “structure-function mapping”. For the conjunctive hypothesis and the structure-function mapping hypotheses, the “realistic” parameter sets were used, while the optimal parameter set was used for the repetition-suppression hypothesis; for values of the parameters, see Table 1. (C) Path hexasymmetry does not depend on the rotation angle of the trajectory. In (B) and (C), lines represent the mean and shaded areas represent the standard error as obtained from 20 random walk trajectories with the same parameters as in Table 1.